



HAL
open science

Early-Time Observations of SN 2023wrk: A Luminous Type Ia Supernova with Significant Unburned Carbon in the Outer Ejecta

Jialian Liu, Xiaofeng Wang, Cristina Andrade, Pierre-Alexandre Duverne, Jujia Zhang, Liping Li, Zhenyu Wang, Felipe Navarete, Andrea Reguitti, Stefan Schuldt, et al.

► **To cite this version:**

Jialian Liu, Xiaofeng Wang, Cristina Andrade, Pierre-Alexandre Duverne, Jujia Zhang, et al.. Early-Time Observations of SN 2023wrk: A Luminous Type Ia Supernova with Significant Unburned Carbon in the Outer Ejecta. *Astrophys.J.*, 2024, 973 (2), pp.117. 10.3847/1538-4357/ad6600 . hal-04667882

HAL Id: hal-04667882

<https://hal.science/hal-04667882v1>

Submitted on 16 Jan 2025

HAL is a multi-disciplinary open access archive for the deposit and dissemination of scientific research documents, whether they are published or not. The documents may come from teaching and research institutions in France or abroad, or from public or private research centers.








L'archive ouverte pluridisciplinaire **HAL**, est destinée au dépôt et à la diffusion de documents scientifiques de niveau recherche, publiés ou non, émanant des établissements d'enseignement et de recherche français ou étrangers, des laboratoires publics ou privés.



Distributed under a Creative Commons Attribution 4.0 International License



Early-time Observations of SN 2023wrk: A Luminous Type Ia Supernova with Significant Unburned Carbon in the Outer Ejecta

Jialian Liu¹ , Xiaofeng Wang¹ , Cristina Andrade² , Pierre-Alexandre Duverne³ , Jujia Zhang^{4,5,6} , Liping Li^{4,5,6} , Zhenyu Wang^{4,5,6,7} , Felipe Navarete⁸ , Andrea Reguitti^{9,10} , Stefan Schuldt^{11,12} , Yongzhi Cai^{4,5,6} , Alexei V. Filippenko¹³ , Yi Yang^{1,13} , Thomas G. Brink¹³ , WeiKang Zheng¹³ , Ali Esamdin¹⁴ , Abdusamatjan Iskandar^{14,15} , Chunhai Bai¹⁴ , Jinzhong Liu¹⁴ , Xin Li¹⁶ , Maokai Hu¹ , Gaici Li¹ , Wenxiong Li¹⁷ , Xiaoran Ma¹ , Shengyu Yan¹ , Jun Mo¹ , Christophe Adami¹⁸ , Dalya Akl¹⁹ , Sarah Antier²⁰ , Eric Broens²¹ , Jean-Grégoire Ducoin²² , Eslam Elhosseiny²³ , Thomas M. Esposito¹³ , Michael Freeberg^{24,25} , Priyadarshini Gokuldass²⁶ , Patrice Hello²⁷ , Sergey Karpov²⁸ , Isabel Márquez²⁹ , Martin Mašek³⁰ , Oleksandra Pyshna³¹ , Yodgor Rajabov³² , Denis Saint-Gelais³³ , Marc Serrau³⁴ , Oleksii Sokoliuk^{35,36} , Ali Takey²³ , Manasanun Tanasan³⁷ , and Damien Turpin³⁸

¹ Physics Department, Tsinghua University, Beijing 100084, People's Republic of China; liu-ji22@mails.tsinghua.edu.cn, wang_xf@mail.tsinghua.edu.cn

² School of Physics and Astronomy, University of Minnesota, Minneapolis, MN 55455, USA

³ Université Paris Cité, CNRS, Astroparticule et Cosmologie, F-75013 Paris, France

⁴ Yunnan Observatories, Chinese Academy of Sciences, Kunming 650216, People's Republic of China

⁵ International Centre of Supernovae, Yunnan Key Laboratory, Kunming 650216, People's Republic of China

⁶ Key Laboratory for the Structure and Evolution of Celestial Objects, Chinese Academy of Sciences, Kunming 650216, People's Republic of China

⁷ University of Chinese Academy of Sciences, Beijing 100049, People's Republic of China

⁸ SOAR Telescope/NSF's NOIRLab Avda Juan Cisternas 1500, 1700000 La Serena, Chile

⁹ INAF—Osservatorio Astronomico di Brera, Via E. Bianchi 46, 23807 Merate (LC), Italy

¹⁰ INAF—Osservatorio Astronomico di Padova, Vicolo dell'Osservatorio 5, 35122 Padova, Italy

¹¹ Dipartimento di Fisica, Università degli Studi di Milano, via Celoria 16, I-20133 Milano, Italy

¹² INAF—IASF Milano, via A. Corti 12, I-20133 Milano, Italy

¹³ Department of Astronomy, University of California, Berkeley, CA 94720-3411, USA

¹⁴ Xinjiang Astronomical Observatory, Chinese Academy of Sciences, Urumqi, Xinjiang 830011, People's Republic of China

¹⁵ School of Astronomy and Space Science, University of Chinese Academy of Sciences, Beijing 100049, People's Republic of China

¹⁶ Beijing Planetarium, Beijing Academy of Science and Technology, Beijing 100044, People's Republic of China

¹⁷ National Astronomical Observatories of China, Chinese Academy of Sciences, Beijing 100012, People's Republic of China

¹⁸ Aix Marseille Univ, CNRS, CNES, LAM, Marseille, France

¹⁹ Physics Department, American University of Sharjah, Sharjah, UAE

²⁰ Université Côte d'Azur, Observatoire de la Côte d'Azur, CNRS, Laboratoire J.-L. Lagrange, Boulevard de l'Observatoire, 06304 Nice, France

²¹ KNC, Vereniging Voor Sterrenkunde, Balen-Neetlaan 18A, B-2400 Mol, Belgium

²² CPPM, Aix Marseille Univ, CNRS/IN2P3, CPPM, Marseille, France

²³ National Research Institute of Astronomy and Geophysics (NRIAG), 1 El-marsad St., 11421 Helwan, Cairo, Egypt

²⁴ KNC, AAVSO, Hidden Valley Observatory (HVO), Colfax, WI 54730, USA

²⁵ iTelescope, Utah Desert Remote Observatory, Beryl Junction, UT 84714, USA

²⁶ Department of Physical Sciences, College of Arts and Sciences, Embry-Riddle Aeronautical University, Daytona Beach, FL 32114, USA

²⁷ IJCLab, Univ Paris-Saclay, CNRS/IN2P3, Orsay, France

²⁸ CEICO, Institute of Physics of the Czech Academy of Sciences, Na Slovance 1999/2, CZ-182 21 Praha, Czech Republic

²⁹ Instituto de Astrofísica de Andalucía (IAA-CSIC), Glorieta de la Astronomía, 18008 Granada, Spain

³⁰ FZU—Institute of Physics, Czech Academy of Sciences, Na Slovance 1999/2, CZ-182 21 Praha, Czech Republic

³¹ The Astronomical observatory of Taras Shevchenko National University of Kyiv, Ukraine

³² Ulugh Beg Astronomical Institute, Uzbekistan Academy of Sciences, Astronomy Str. 33, Tashkent 100052, Uzbekistan

³³ KNC, Sociedad Astronómica Queretana, Mexico, RAPAS Observatoire de Paris, France, Le club des Astronome Amateur de Rosemère du Québec, Canada

³⁴ KNC, Société Astronomique de France, Observatoire de Dauban, F-04150 Banon, France

³⁵ Astronomical Observatory of Taras Shevchenko National University of Kyiv, Observatorna Str. 3, Kyiv, 04053, Ukraine

³⁶ Main Astronomical Observatory of National Academy of Sciences of Ukraine, 27 Acad. Zabolotnoho Str., Kyiv 03143, Ukraine

³⁷ National Astronomical Research Institute of Thailand (Public Organization), 260, Moo 4, T. Donkaew, A. Mae Rim, Chiang Mai 50180, Thailand

³⁸ Université Paris-Saclay, Université Paris Cité, CEA, CNRS, AIM, 91191 Gif-sur-Yvette, France

Received 2024 June 15; revised 2024 July 19; accepted 2024 July 19; published 2024 September 25

Abstract

We present extensive photometric and spectroscopic observations of the nearby Type Ia supernova (SN) 2023wrk at a distance of about 40 Mpc. The earliest detection of this SN can be traced back to a few hours after the explosion. Within the first few days, the light curve shows a bump feature, while the $B - V$ color is blue and remains nearly constant. The overall spectral evolution is similar to that of an SN 1991T/SN 1999aa-like SN Ia, while the C II $\lambda 6580$ absorption line appears to be unusually strong in the first spectrum taken at $t \approx -15.4$ days after the maximum light. This carbon feature disappears quickly in subsequent evolution but it reappears at around the time of peak brightness. The complex evolution of the carbon line and the possible detection of Ni III absorption around 4700 Å and 5300 Å in the earliest spectra indicate macroscopic mixing of fuel and ash. The strong carbon lines are likely related to the collision of SN ejecta with unbound carbon, consistent with the predictions of pulsational delayed-detonation or

carbon-rich circumstellar-matter interaction models. Among those carbon-rich SNe Ia with strong C II $\lambda 6580$ absorption at very early times, the line-strength ratio of C II to Si II and the $B - V$ color evolution are found to exhibit large diversity, which may be attributed to different properties of unbound carbon and outward-mixing ^{56}Ni .

Unified Astronomy Thesaurus concepts: Type Ia supernovae (1728)

Materials only available in the [online version of record](#): machine-readable tables

1. Introduction

Type Ia supernovae (SNe Ia; see, e.g., Filippenko 1997 for a review of SN classification) are widely believed to arise from thermonuclear explosions of carbon-oxygen (C/O) white dwarfs (WDs) (Nomoto et al. 1997; Hillebrandt & Niemeyer 2000). Thanks to the high peak luminosity and width-luminosity relation of their light curves (WLR, also dubbed the “Phillips relation”; Phillips 1993; Phillips et al. 1999), SNe Ia have been used as standardizable candles in cosmology, playing a critical role in the discovery of the accelerating expansion of the Universe (Riess et al. 1998; Perlmutter et al. 1999) and measurement of the Hubble constant (e.g., Riess et al. 2022; Murakami et al. 2023).

About three decades ago, SNe Ia were classified into spectroscopically peculiar and normal (dubbed as “Branch-normal”) SNe Ia (Branch et al. 1993). Later, more diversity has been noticed for SNe Ia, even among the normal ones. For example, Benetti et al. (2005) found that SNe Ia could be divided into low-velocity-gradient (LVG) and high-velocity-gradient (HVG) objects according to the velocity gradient measured from the Si II $\lambda 6355$ absorption, and this velocity gradient is not correlated with $\Delta m_{15}(B)$ (Phillips 1993) for normal SNe Ia. Branch et al. (2006) assigned SNe Ia into four groups based on the strengths of their Si II lines: the “shallow silicon” group with a weak Si II $\lambda 6355$ line, the “cool” group with a high line-strength ratio of Si II $\lambda 5972$ to Si II $\lambda 6355$, the “broad-line” group with strong Si II $\lambda 6355$, and the “core-normal” group with a moderate Si II line strength and a high degree of spectral homogeneity. Based on the Si II $\lambda 6355$ velocity, Wang et al. (2009) divided normal SNe Ia into two categories: high velocity (HV) and normal velocity (NV), which may arise from different birth environments (Wang et al. 2013). Wang et al. (2009) found an apparent dichotomy in the host-galaxy reddening law ($R_V = 2.4$ for NV SNe and $R_V = 1.6$ for HV SNe), and concluded that applying such an absorption-correction dichotomy could significantly reduce the peak luminosity dispersion. Some subtypes of SNe Ia with peculiar properties compared with normal objects have also been found, such as the luminous SN 1991T-like or SN 1999aa-like (hereafter 91T/99aa-like, which belong to the Branch “shallow silicon” subclass) objects (Filippenko et al. 1992; Phillips et al. 1992; Krisciunas et al. 2000), the subluminous SN 1991bg-like (hereafter 91bg-like, which belong to the Branch “cool” subclass) objects (Filippenko et al. 1992; Leibundgut et al. 1993), the super-Chandrasekhar-mass SN 2003fg-like objects (Howell et al. 2006), and the moderately declining, subluminous SN 2002es-like objects (Ganeshalingam et al. 2012).

Among different subtypes of SNe Ia, the 91T/99aa-like objects are characterized by prominent Fe II/III absorption and weak Si II $\lambda 6355$ absorption in the early-time spectra; 91T-like SNe are systematically more luminous than 99aa-like and “normal” SNe Ia with similar decline rates (Boone et al. 2021; Phillips et al. 2022; Yang et al. 2022). This has been explained by more complete burning, more nickel synthesized in their

explosions, and the resulting higher photospheric temperature (Saselli et al. 2014). Phillips et al. (2022) also emphasized that the postpeak decline rate alone cannot be used to differentiate between 91T-like, 99aa-like, and luminous SNe Ia with “normal” spectra. Although the fraction of 91T/99aa-like SNe Ia in the local universe is estimated to be low ($\sim 4\%$ in the ASASSN survey (Desai et al. 2024) and $\sim 5\%$ in X. Ma et al. 2024, in preparation), this fraction could increase in the distant universe owing to a shorter delay time of formation (Chakraborty et al. 2024). Moreover, the 91T/99aa-like objects could extend the cosmological sample to higher redshifts (Yang et al. 2022) because of their relatively high luminosity. However, it is still debated whether 91T/99aa-like objects and normal subclasses arise from a common progenitor system and explosion mechanism and follow exactly the same WLR. The spectra of 91T/99aa-like SNe Ia progressively resemble those of the normal ones around and beyond the time of peak brightness. Moreover, SN 1999aa exhibits some properties intermediate between those of SN 1991T and normal SNe Ia, and SN 1999aa is more similar to normal SNe Ia at earlier phases and shows prominent Ca II H&K lines that are not seen in SN 1991T (Garavini et al. 2004). But these luminous SNe Ia could introduce systematic biases when inferring cosmological distances with them (Scalzo et al. 2012).

Although having relatively high peak luminosities and slowly evolving light curves, there have not been many observations of 91T/99aa-like objects at very early times, which are important for constraining their progenitor systems and explosion mechanisms. Exceptions to this include iPTF14bdn (Smitka et al. 2015) and iPTF16abc (Miller et al. 2018; Aouad et al. 2024). But besides the weak Si II and strong Fe III absorption, iPTF16abc also has a prominent and short-lived C II $\lambda 6580$ line that is even stronger than Si II $\lambda 6355$ at $t \approx -15$ days and disappears at $t \approx -7$ days relative to B -band maximum, indicating a more complicated diversity among 91T/99aa-like objects.

Miller et al. (2018) find that the pulsational delayed-detonation (PDDEL) models of Dessart et al. (2014) provide a good match to the early carbon features but a bad match to the “bump” in the light curve of iPTF16abc. In comparison with a typical SN Ia (e.g., SN 2011fe; Zhai et al. 2016), spectroscopic and photometric observations show a very blue spectral energy distribution (SED) for iPTF16abc at very early times. The collision of SN ejecta with a nondegenerate companion (Kasen 2010) can produce an early blue bump, but this scenario is excluded for iPTF16abc by Miller et al. (2018) based on the early light curves. Other possible scenarios, including ^{56}Ni mixing such that its distribution does not decrease monotonically toward the outer ejecta (e.g., Shappee et al. 2019; Magee & Maguire 2020) and ejecta interaction with circumstellar matter (CSM; e.g., Hu et al. 2023; Maeda et al. 2023; Moriya et al. 2023), need further exploration. The reappearance of C II $\lambda 6580$ after B -band maximum is also an interesting characteristic of iPTF16abc (Aouad et al. 2024), which is also seen in SN 2018oh (a normal SN Ia with an early flux excess; Li & Wang 2019). This

reappearing carbon distinguishes iPTF16abc from 03fg-like or 02es-like objects, which have strong and long-lasting carbon features (e.g., 03fg-like SN 2020esm, Dimitriadis et al. 2022; 02es-like iPTF14atg, Cao et al. 2015).

Some slow decliners among normal SNe Ia, such as SN 2012cg (Silverman et al. 2012; Marion & Brown 2016) and SN 2013dy (Zheng et al. 2013; Pan et al. 2015), share a few properties with the 91T/99aa-like subclass, including low-velocity gradient and shallow silicon lines. Their spectra exhibit intermediate-mass elements (IMEs; e.g., Si II $\lambda 6355$) with moderate line strengths lying between those of 91T/99aa-like and other normal SNe Ia. In particular, strong C II $\lambda 6580$ absorption, comparable to the Si II $\lambda 6355$ line, is seen in the early-time spectra of both SN 2012cg and SN 2013dy, while it is usually weak or absent in normal SNe Ia (e.g., SN 2011fe; Nugent et al. 2011; Zhang et al. 2016). Combining this with the reappearing carbon feature seen in SN 2018oh, the 91T/99aa-like objects and normal SNe Ia may share the peculiar evolution of carbon absorption and thus a similar progenitor system and explosion mechanism. More 91T/99aa-like SNe Ia with very early observations are needed to study their origins and their potential connections with normal SNe Ia.

In this paper, we present extensive photometry and spectroscopy of SN 2023wrk, a 91T/99aa-like SN Ia. The observations are described in Section 2. We analyze the light curves and spectra in Sections 3 and 4, respectively. A discussion is given in Section 5, and we summarize in Section 6.

2. Observations and Data Reduction

SN 2023wrk was discovered (Godson et al. 2023) on 2023 November 4 (UTC dates are used throughout this paper; MJD 60252.233) by the Gravitational-wave Optical Transient Observer (GOTO) at $\alpha = 11^{\text{h}}28^{\text{m}}39.166^{\text{s}}$, $\delta = 58^{\circ}33'12''.68$ (J2000), just ~ 0.7 d after the last nondetection by the Zwicky Transient Facility (ZTF) on MJD 60251.516. Note that ZTF has a 3σ detection on MJD 60251.523, as shown in Figure 1, where the ZTF difference images in the insets are taken from IRSA (IRSA 2022). The object was then classified as an SN Ia based on a spectrum taken with YFOSC (Wang et al. 2019) on the Lijiang 2.4 m telescope (LJT; Fan et al. 2015) of Yunnan Astronomical Observatories the day after discovery (Li et al. 2023). The prominent feature at ~ 6250 Å comes from C II $\lambda 6580$ instead of Si II $\lambda 6355$, which may have led to the wrong estimated redshift by Li et al. (2023). The interstellar Na I D absorption shows that the merging binary galaxy NGC 3690 is the host of SN 2023wrk (see Section 3.1). As noted in Arrizabalaga-Díaz-Caneja (2023), SN 2023wrk is the first thermonuclear SN explosion in this extremely productive galaxy that has produced more than 15 SNe over the past 30 yr.

2.1. Photometry

After the discovery, we performed timely photometry of SN 2023wrk in *grizBVRI* filters with the LJT, the Nanshan One-meter Wide-field Telescope (NOWT; Bai et al. 2020) at Nanshan Station of Xinjiang Astronomical Observatory, the 0.8 m Tsinghua University-NAOC Telescope (TNT; Wang et al. 2008; Huang et al. 2012) at Xinglong Station of NAOC, and the Schmidt 67/91 cm Telescope (67/91-ST) and the 1.82 m Copernico Telescope (Copernico) at the Mount Ekar Observa-

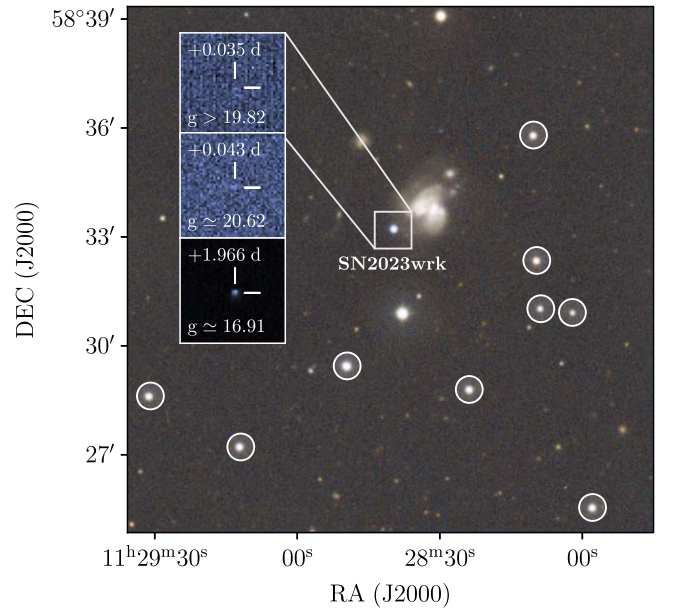


Figure 1. Schmidt 67/91 cm telescope 14.5×14.5 color composite (*B/V/r*) image of SN 2023wrk and its host galaxy. The reference stars used to calibrate the photometry are marked with circles. The insets show the zoomed-in region of three ZTF difference images from IRSA, centered on the SN location, taken at phases of $t \approx +0.035$, $+0.043$, and $+1.966$ days relative to the time of first light (MJD 60251.48; see Section 3.2). The top inset gives a 5σ limit.

We also triggered the Global Rapid Advanced Network Devoted to the Multi-messenger Addict (GRANDMA) to observe SN 2023wrk since 2023 November 6. GRANDMA is a network of ground-based facilities dedicated to time-domain astronomy focused on electromagnetic follow-up observations of gravitational-wave progenitors and other transients. The network contains 36 telescopes from 30 observatories, 42 institutions, and groups from 20 countries. GRANDMA utilizes wide and narrow field-of-view telescopes distributed across all continents (Antier et al. 2020, 2020; Aivazyan et al. 2022; Kann et al. 2023). GRANDMA’s network extends to its citizen science project entitled Kilonova-Catcher (KNC),³⁹ allowing amateur astronomers to contribute to GRANDMA campaigns.

All of these images were preprocessed following standard routines, including bias subtraction, flat-field correction, dark-current correction, and cosmic-ray removal. We have used AUTOPHOT (Brennan & Fraser 2022) to perform aperture or point-spread-function photometry for the LJT, NOWT, TNT, 67/91-ST, and Copernico images. Aperture photometry was conducted for GRANDMA images using the Python package STDPipe⁴⁰ (Karpov 2021). The instrumental magnitudes were calibrated using the Gaia Synthetic Photometry Catalogue (Collaboration et al. 2023) for *UBVRI* filters, the Pan-STARRS Release 1 (Chambers et al. 2016) for *griz* filters, and the Sloan Digital Sky Survey Release 16 (Ahumada et al. 2020) for the *u* filter. In addition, the unfiltered images of KNC-Unistellar span a wide band from near-ultraviolet (near-UV) to near-infrared (NIR), posing challenges for standard calibration. We addressed these images by using the *G* band of the Gaia eDR3 catalog (Collaboration et al. 2023) because it covers a range of wavelengths similar to that of the Unistellar instruments (visible

³⁹ <http://kilonovacatcher.in2p3.fr/>

⁴⁰ <https://gitlab.in2p3.fr/icare/stdpipe>

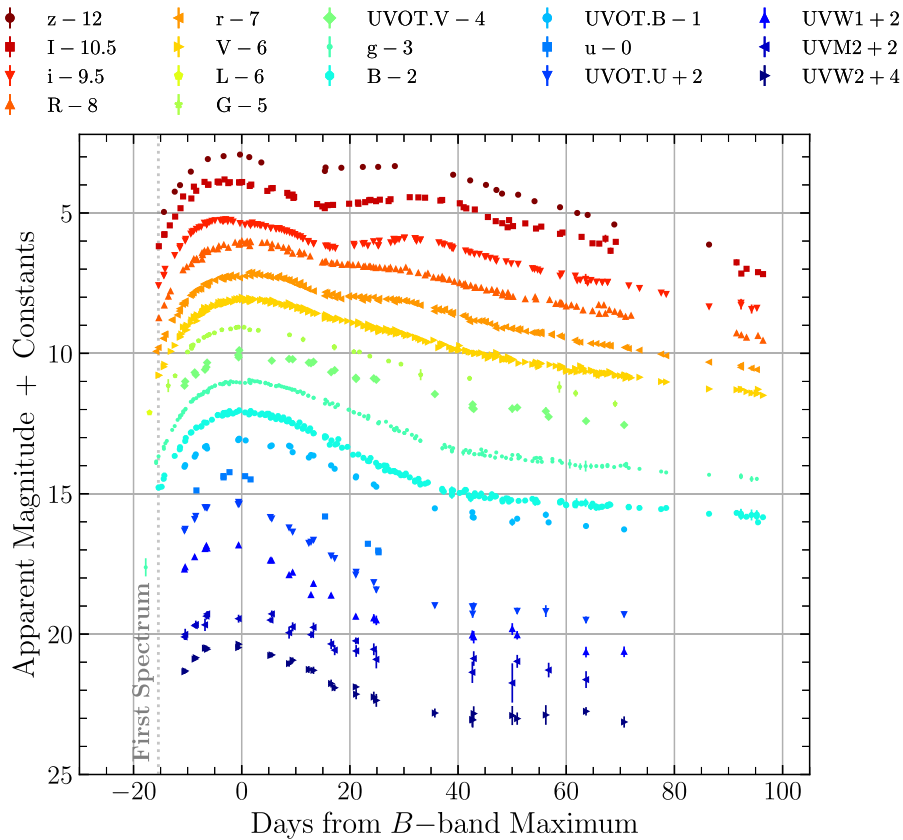


Figure 2. UV and optical light curves of SN 2023wrk. The phase is relative to the B -band maximum (MJD = 60269.45, see Section 3.3). Data in different filters are shown with different colors and shapes, and are shifted vertically for better display, as indicated in the top legend. No S correction (e.g., see Stritzinger et al. 2002) has been applied to the data points plotted in this figure.

through NIR). This resulted in a color-term correction below 0.1 mag, rendering it negligible.

SN 2023wrk was also observed by the Ultraviolet/Optical Telescope (UVOT; Gehrels et al. 2004; Roming et al. 2005) on the Neil Gehrels Swift Observatory (Gehrels et al. 2004) in three UV ($UVW2$, $UVM2$, $UVW1$) and three optical (U , B , V) filters. We extracted Swift photometry using HEASOFT⁴¹ with the latest Swift calibration database.⁴² In addition, we include the g - and r -band photometry of ZTF provided by Lasair.⁴³

All the light curves of SN 2023wrk are shown in Figure 2. A summary of the photometric observations triggered by us is presented in Appendix A, including telescope names and the corresponding filters and number of images. The photometry is also presented in Appendix A.

2.2. Spectroscopy

Optical spectra of SN 2023wrk were collected with several different instruments, including BFOSC mounted on the Xinglong 2.16 m telescope (XLT; Zhang et al. 2016), YFOSC on LJT, AFOSC on Copernico, LRIS (Oke et al. 1995) on the 10 m Keck I telescope on Maunakea, Kast double spectrograph (Miller & Stone 1994) and HIRES on the 3 m Shane telescope at Lick Observatory; MISTRAL on the 1.93 m telescope at Observatoire de Haute Provence (OHP), DOLoRES-LRS on Telescopio Nazionale Galileo (TNG) on

the island of La Palma, and two amateur telescopes EBE and ESOU of KNC. The Keck I/LRIS spectrum was reduced using the LPIpe pipeline (Perley 2019). The standard IRAF⁴⁴ routines were used to reduce other spectra. Flux calibration of the spectra was performed with spectrophotometric standard stars observed on the same nights. Atmospheric extinction was corrected with the extinction curves of local observatories. We derived the telluric correction using the spectrophotometric standard star. A journal of spectroscopic observations of SN 2023wrk is presented in Appendix B, and all the spectra are displayed in Figure 3. These spectra are available in the Weizmann Interactive Supernova Data Repository (WiSeREP).⁴⁵

3. Photometry

3.1. Reddening and Distance

Interstellar Na I D absorptions with a redshift $z \approx 0.01$ can be clearly seen and should be from the host binary galaxy NGC 3690 ($z = 0.0104$; NASA/IPAC Extragalactic Database (NED), 2019). The Galactic reddening is estimated to be $E(B - V)_{\text{Gal}} = 0.014$ mag (Schlafly & Finkbeiner (2011)). The equivalent width (EW) of Na I D absorption due to the host galaxy can be used to estimate the host reddening using the empirical relation $\log_{10}(E(B - V)) = 1.17 \times \text{EW}(D_1 + D_2) - 1.85$ (Poznanski et al. 2012). Rather than deriving the host reddening directly from this

⁴¹ HEASOFT, the High Energy Astrophysics Software, <https://www.swift.ac.uk/analysis/software.php>.

⁴² <https://heasarc.gsfc.nasa.gov/docs/heasarc/caldb/swift/>

⁴³ <https://lasair-ztf.lsst.ac.uk>

⁴⁴ IRAF is distributed by the National Optical Astronomy Observatories, which are operated by the Association of Universities for Research in Astronomy, Inc., under cooperative agreement with the National Science Foundation (NSF).

⁴⁵ <https://www.wiserep.org/>

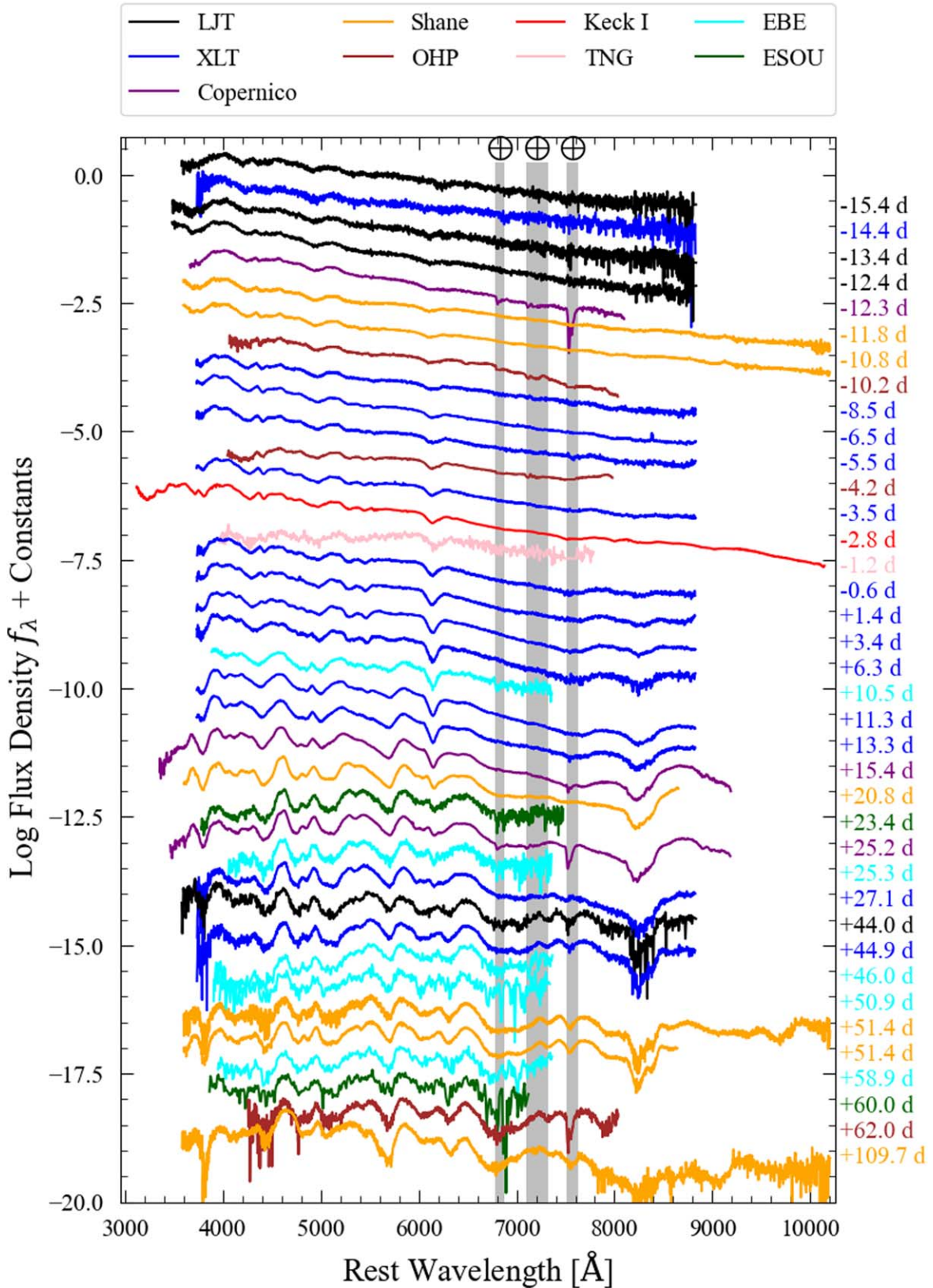


Figure 3. Optical spectral evolution of SN 2023wrk from -15.4 to $+109.7$ days relative to B -band maximum light. All spectra have been corrected for reddening and host-galaxy redshift. Spectra taken with different telescopes are in different colors as indicated in the top legend. The phase of each spectrum is shown on the right side. Regions of the main telluric absorption are marked by gray vertical bands.

empirical relation, we estimate it by comparing the EWs of the Na I D absorption due to the Milky Way and the host galaxy. With the spectrum taken at $t \approx -4.2$ days, we measure EWs of

$0.33 \pm 0.03 \text{ \AA}$ and $0.58 \pm 0.05 \text{ \AA}$ for the Milky Way and the host-galaxy components, respectively. Using the empirical relation of Poznanski et al. (2012) and assuming

$E(B - V)_{\text{Gal}} = 0.014$ mag, we obtain a host-galaxy reddening of $E(B - V)_{\text{host}} = 0.028 \pm 0.020$ mag for which we add a $\sim 68\%$ error as suggested by Phillips et al. (2013). Note that the reddening directly derived from the empirical relation is larger but still within the uncertainty, with $E(B - V)_{\text{Gal}} = 0.034 \pm 0.023$ mag and $E(B - V)_{\text{host}} = 0.067 \pm 0.046$ mag. We adopt a host reddening of 0.028 mag and a total reddening of 0.042 mag in our analysis. Assuming $H_0 = 73 \pm 5$ km s $^{-1}$ Mpc $^{-1}$ (the value is taken from Riess et al. (2022) and the uncertainty considers the Hubble tension) and correcting for peculiar motions related to the Virgo cluster and Great Attractor (Mould et al. 2000), the distance to NGC 3690 is estimated to be 48.25 ± 3.32 Mpc, with the corresponding distance modulus 33.42 ± 0.15 mag.

3.2. Time of First Light

To estimate the time of first light, we fit a power law to our early data in g ,

$$F_g = A(t - t_0)^\alpha, \quad (1)$$

where F_g is the flux density in the g band, A is the scale factor, t_0 is the time of first light, and α is the power-law index. Following Miller et al. (2018), we fit the data within the first 3 days; this yields $t_0 = 60251.48 \pm 0.04$ (MJD) and $\alpha = 0.92 \pm 0.17$. We fail to obtain the built-in samples using MCMC Hammer EMCEE (Foreman-Mackey et al. 2013), so the reported uncertainty is from the parameter covariances. The fitting results are shown in the top panel of Figure 4, where we add the g -band data of iPTF16abc for comparison. We find that the g light curve of SN 2023wrk follows a power-law evolution with $\alpha \approx 1$, similar to iPTF16abc (Miller et al. 2018). This indicates that SN 2023wrk exhibits a prominent flux excess in the first few days, as does iPTF16abc. According to the fitting, the first ZTF observation of SN 2023wrk was taken only ~ 0.05 days after first light. We also apply a power-law fit using g -band data obtained within 4–7 days after first light, when the SN flux is $\lesssim 40\%$ of the peak and the flux excess is negligible. The best fit is shown in the bottom panel of Figure 4, and it gives $t_0 = 60251.29$ and $\alpha = 1.75$. In this case, the first point of SN 2023wrk is ~ 0.1 days later than that of iPTF16abc but with a lower flux. We find that EMCEE gives $t_0 = 60251.09_{-0.37}^{+0.31}$ and $n = 1.80_{-0.10}^{+0.12}$ based on the 16th, 50th, and 84th percentiles of the samples in the marginalized distributions. Such a first-light time derived from the linear fit to the first three days should be more accurate, since the epoch of the first detection is very close to that of the last nondetection. Moreover, a linear rise of early-phase flux has been observed in many SNe Ia with early excess emission (Jiang et al. 2018). Thus, we adopt the first-light time as MJD 60251.48 ± 0.04 in this paper.

3.3. Optical Light Curve

We applied a fifth-order polynomial fit to the B - and V -band light curves around maximum light and find that SN 2023wrk reached a peak magnitude of $B_{\text{max}} = 14.08 \pm 0.01$ mag on 2023 November 21.45 \pm 0.10 (MJD = 60269.45 \pm 0.10) with $\Delta m_{15}(B) = 0.87 \pm 0.02$ mag, and $V_{\text{max}} = 14.08 \pm 0.01$ mag on 2023 November 22.46 \pm 0.10 (MJD = 60270.46 \pm 0.10) with $\Delta m_{15}(V) = 0.62 \pm 0.01$ mag; these are adopted throughout this paper. The rise time in B is $t_r^B = 17.79 \pm 0.11$ days, consistent

with that of iPTF16abc ($t_r^B = 17.91 \pm_{0.15}^{0.07}$ days). Assuming $R_B = 4.1$ and a total reddening of $E(B - V) = 0.042$ mag, the B -band absolute peak magnitude is $M_{\text{max}}(B) = -19.51 \pm 0.15$ mag.

In Figure 5, we compare the absolute B , g , V , and r light curves of SN 2023wrk and some well-observed SNe Ia, including the typical normal SN 2011fe ($\Delta m_{15}(B) = 1.18 \pm 0.03$ mag; Zhang et al. 2016), the 91T/99aa-like object iPTF16abc ($\Delta m_{15}(B) = 0.89 \pm 0.01$ mag,⁴⁶ and four normal SNe Ia that have been reported to have early flux excesses: SNe 2012cg ($\Delta m_{15}(B) = 0.91 \pm 0.03$ mag; Stahl et al. 2019), 2013dy ($\Delta m_{15}(B) = 0.87 \pm 0.02$ mag; Stahl et al. 2019), 2017cbv ($\Delta m_{15}(B) = 0.99 \pm 0.01$ mag; Wang et al. 2020), and 2018oh ($\Delta m_{15}(B) = 0.96 \pm 0.03$ mag; Li & Wang 2019). The adopted distance modulus, reddening (assuming $R_V = 3.1$), and first-light time of the comparison SNe Ia can be found in Appendix C. We find that SN 2023wrk has light curves similar to iPTF16abc and the normal SNe Ia with early excesses except for SN 2012cg. In the early phases, SN 2012cg appears obviously fainter than the other four comparison SNe Ia (including SN 2023wrk) having an early excess, though they exhibit similar light curves at around the maximum light. In fact, SN 2012cg only exhibits weak early excesses compared to SN 2011fe. Beyond maximum light, SN 2023wrk, iPTF16abc, and all the normal SNe Ia with early excesses have similar light-curve decline rates that are obviously slower than those of SN 2011fe.

The $B - V$ color evolution is shown in Figure 6, where SN 2023wrk and iPTF16abc (and perhaps SN 1999aa) show a constant blue color until maximum light. Among the comparison sample, SN 2011fe shows a rapid red-blue color evolution at $t \lesssim -10$ days relative to the B maximum, while SNe 1991T, 2012cg, 2013dy, and 2017cbv tend to show a gradual red-to-blue color evolution within the first week after explosion. The overall color evolution of SN 2023wrk is quite similar to that of iPTF16abc, indicating that these two 99aa-like SNe Ia share similar temperature evolution.

4. Spectral Analysis

4.1. Spectral Evolution

We compare the spectra of SN 2023wrk with those of comparison SNe Ia in Figure 7. At $t \approx -15$ days relative to B -band maximum, SN 2023wrk shows prominent Fe III absorption and weak Si II $\lambda 6355$ absorption characteristic of 91T/99aa-like objects, though its Fe III lines are weaker. And it seems that SN 2023wrk is more similar to SN 1999aa as Ca II H&K lines can be clearly seen. In addition, we identify Ni III features in the spectrum of SN 2023wrk by comparing it with the $t \approx -10.7$ days spectrum of SN 1999aa (Garavini et al. 2004), which indicates nickel in the very outer layers. Different from both SNe 1991T and 1999aa, however, SN 2023wrk exhibits strong C II $\lambda 6580$ absorption, which is a characteristic of 03fg-like objects such as SN 2020esm. We notice that all of these features of SN 2023wrk are also found in iPTF16abc, and the SEDs of these two SNe Ia are also extremely similar and much bluer than SN 2011fe at short wavelengths. The spectra of the normal SNe Ia having flux excesses at early times (SNe 2012cg and 2013dy) are also similar to those of SN 2023wrk to some extent, such as the bluer SEDs and weaker Si II lines compared with SN 2011fe, and possible Fe III lines around 4200 Å and

⁴⁶ This value is obtained by applying a fifth-order polynomial fit to the B -band light curve as no $\Delta m_{15}(B)$ value is reported by Miller et al. (2018).

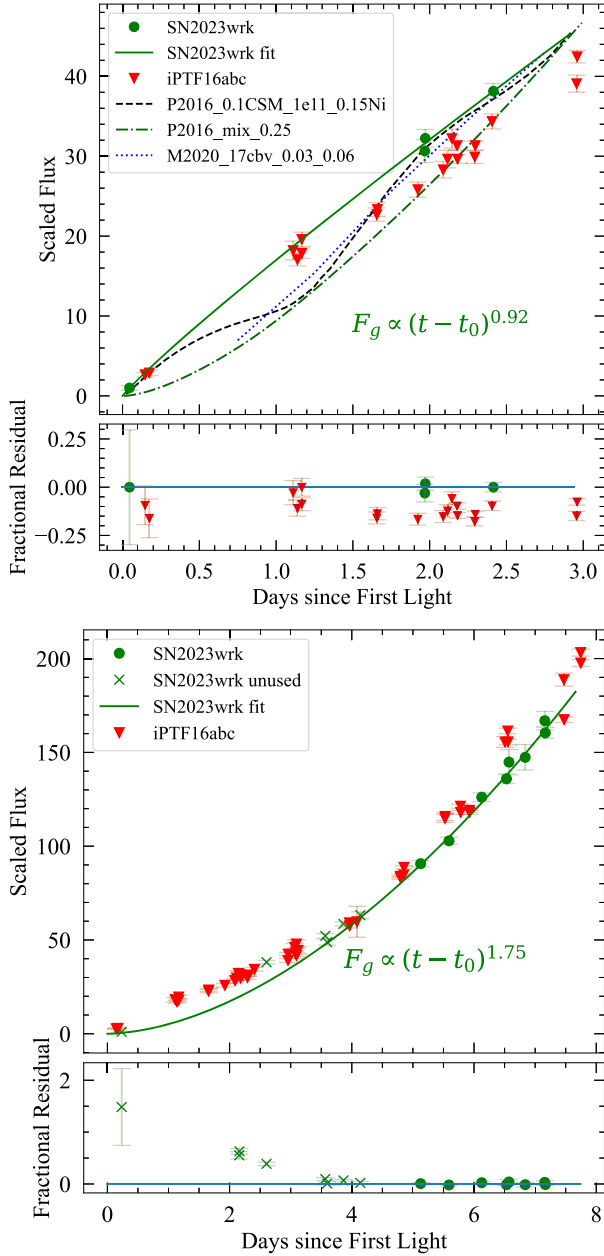


Figure 4. Power-law fits to the early-time g -band light curve of SN 2023wrk. Fits to the data obtained within the first 3 days and the first 7 days are shown in the top and bottom panels, respectively. The g data of SN 2023wrk used to fit the power law are shown in green circles, with the unused data shown in green “x” symbols and the best-fit curve shown as a green line. For comparison, the g data of iPTF16abc are shown as red inverted triangles. The fluxes of SN 2023wrk and iPTF16abc are converted from their absolute magnitudes and are then scaled to the first point of SN 2023wrk. The fractional residual is equal to $(F_{\text{obs}} - F_{\text{fit}})/F_{\text{fit}}$, where F_{obs} is the flux of the observation and F_{fit} is the flux of the fitting curve. In the left panel, we plot the light curves of three models for comparison, and the corresponding parameters and discussions can be found in Section 5.2.1.

4900 Å. But the difference is that their Si II $\lambda 6355$ line is still stronger than that of SN 2023wrk, and their 4900 Å absorption features have a more extended blue wing, which could be attributed to Fe II absorption and thus imply comparable line strengths of Fe II and Fe III.

At $t \approx -7$ days, the C II absorption disappeared in SN 2023wrk and iPTF16abc, while it is still prominent in SN 2020esm. The Si II absorption of SN 2023wrk can be

seen clearly and has a similar line strength to not only iPTF16abc but also SN 1999aa and the normal Ia SN 2013dy, while SN 1991T still shows no evident Si II absorption. The profile of the 4900 Å absorption feature of SN 2023wrk is still different from those of normal SNe Ia with early excesses, especially SN 2018oh, which has two visible absorption troughs.

At around the peak brightness, the C II absorption reappeared in SN 2023wrk and iPTF16abc. The spectra of SN 2023wrk resemble those of SNe 2012cg, 2018oh, and even SN 2011fe though the SED is still different in short wavelength. The good wavelength coverage of the LRIS spectrum of SN 2023wrk at $t \approx -2.8$ days allows us to find an absorption feature in the blue side of Ca II H&K. In contrast to SN 1999aa, this absorption is weaker than that of Ca II H&K and can be just attributed to Co III and Si III rather than HV Ca II H&K (Aouad et al. 2024). We also find Co III and Co II lines at $\lesssim 4000$ Å in the LRIS spectrum. The reappearing C II absorption of SN 2023wrk can still be seen at $t \approx +20.8$ days and finally disappeared at $t \approx +25.2$ days.

One of the most interesting spectral features in SN 2023wrk is the evolution of the Si II $\lambda 6355$ and C II $\lambda 6580$ lines. To better examine this evolution, Figure 8 shows the 5800–6600 Å region spanning phases from -15.4 to $+11.3$ days relative to B -band maximum brightness, overplotted with the spectra of iPTF16abc at comparable phases. At $t \approx -15.4$ days, the Si II absorption is nearly absent, while the C II line is prominent with a velocity of $\sim 15,500$ km s $^{-1}$. One day later, the Si II line becomes prominent with a velocity of $\sim 14,000$ km s $^{-1}$, while the C II line becomes progressively weaker within a few days and tends to disappear by $t \approx -7$ days. Interestingly, the C II absorption becomes visible again in the $t \approx -3.7$ days and -2.9 days spectra, and it grows even stronger at $t \approx +6.3$ days. By $t \approx +25$ days, the C II line finally disappears in the spectra (see Figure 7).

In summary, the spectra of SN 2023wrk are overall quite similar to those of iPTF16abc, with characteristics of 91T/99aa-like objects and a complex evolution of the C II absorption. Together with the similar photometric properties, it is likely that SN 2023wrk and iPTF16abc can be regarded as twin objects.

4.2. Line Velocities

To better measure the line velocities of SN 2023wrk, we first smooth the spectra with a Savitsky–Golay filter (Savitzky & Golay 1964) of order 1 and appropriate width⁴⁷ and then normalize the spectra with a local pseudocontinuum for each feature. The pseudocontinuum points connecting the red and blue sides of the features are chosen interactively. The ejecta velocities are measured from the local absorption minimum of the features. The associated uncertainties are estimated by the standard deviation of a Monte Carlo sample, where we randomly vary the endpoints of the pseudocontinuum within 10 Å and the filter width within an appropriate range where the line feature is not overly smoothed.

For SN 2023wrk, the ejecta velocities inferred from absorption lines of different species are shown in the top panel of Figure 9. The Si II $\lambda 6355$ velocity is measured as $10,100 \pm 100$ km s $^{-1}$ around the time of maximum light, and the velocity gradient is found to be 31 ± 12 km s $^{-1}$ day $^{-1}$ by fitting a linear function from $t \approx +0$ to $\sim +10$ days relative to B -band maximum. This puts SN 2023wrk in the NV (Wang et al. 2009) and LVG subgroups (Benetti et al. 2005). At $t \lesssim -10$ days, the C II $\lambda 6580$ line has a

⁴⁷ We increase the filter width gradually until the minimum of the feature can be clearly identified.

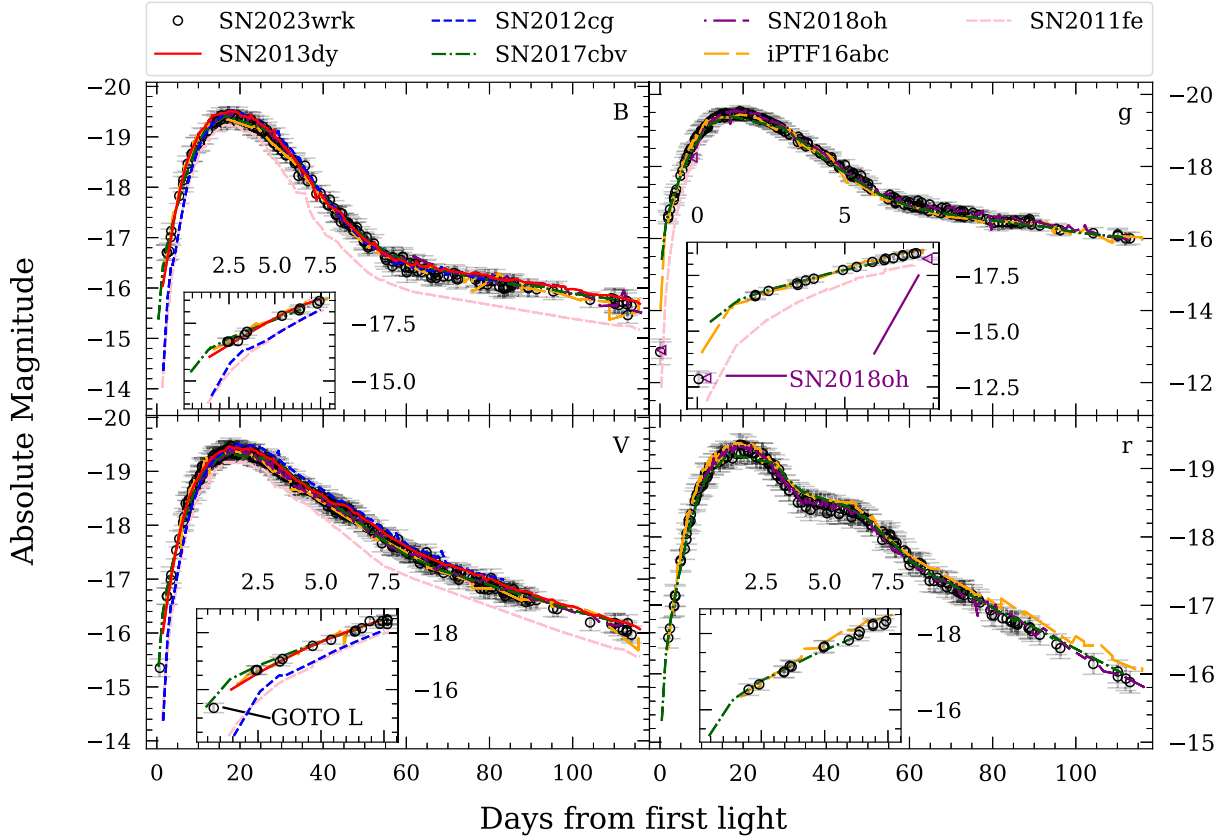


Figure 5. Light-curve comparison of SN 2023wrk with SNe 2011fe (Nugent et al. 2011; Firth et al. 2015; Zhang et al. 2016), 2012cg (Stahl et al. 2019), 2013dy (Zheng et al. 2013; Pan et al. 2015), 2017cbv (Burns et al. 2020), 2018oh (Li & Wang 2019), and iPTF16abc (Miller et al. 2018). The first L -band detection by GOTO is plotted in the V -band subplot, as these two bands have a similar effective wavelength. The light curve of each object has been corrected for the reddening reported in the corresponding reference.

velocity larger than that inferred from Si II $\lambda 6355$, while at $t \gtrsim +5$ days the carbon velocity seems to experience a sudden drop, suggesting that the carbon in SN 2023wrk has a wider distribution than the silicon. In contrast with the nearly constant velocity of Si II after the peak light, the Fe III $\lambda 4404$ line shows a rapid velocity decline, similar to that of iPTF16abc (Aouad et al. 2024) and other 91T/99aa-like objects (Garavini et al. 2004). We summarize some basic photometric and spectroscopic parameters of SN 2023wrk in Table 1.

In the bottom panel of Figure 9, we show the Si II $\lambda 6355$ velocity evolution for SN 2023wrk and the comparison sample. At $t \lesssim -14$ days, SNe 2012cg, 2013dy, iPTF16abc, and 2023wrk show larger velocities and also decline faster than SN 2011fe. The Si II velocity of SN 2023wrk and iPTF16abc shows a plateau-like evolution during phases from $t \approx -13.5$ to -8.5 days relative to B -band maximum. A similar Si II velocity evolution may be also seen in SN 2013dy at $t \approx -10$ days. This velocity plateau may result from a spike structure in the density profile in velocity space and will be discussed in Section 5.2.3.

5. Discussion

5.1. Pseudobolometric Light Curve

We compute the pseudobolometric light curve of SN 2023wrk using Swift $UVW2$, $UVM2$, $UVW1$, U , and ground-based $BgVriz$ photometry. The data are interpolated in each filter so that the bolometric luminosity can be calculated at the same phase. Using SNooPy2 (Burns et al. 2011), the flux from ~ 2000 to 8800 \AA is estimated with the direct integrating method, and the flux from

~ 8800 to 24000 \AA is estimated with the SED method based on the template spectra from Hsiao et al. (2007), since we do not have NIR data. To check whether our estimate of the NIR flux is reliable, we compare the flux density of the photometry, the template spectra mangled by the photometry of SN 2023wrk, the LRIS spectrum ($3150\text{--}10250 \text{ \AA}$) of SN 2023wrk, and a synthetic spectrum of the PDEDEL1 model (Dessart et al. 2014) at $t \approx -3$ days. We find that the $\sim 9000\text{--}10000 \text{ \AA}$ region of the mangled template spectrum is close to that of SN 2023wrk, and the $\gtrsim 10000 \text{ \AA}$ region of the mangled template spectrum is comparable to that of the PDEDEL1 spectrum, which agrees well with SN 2023wrk at $\gtrsim 5000 \text{ \AA}$. These comparisons favor our estimation of the NIR flux of SN 2023wrk. Then we obtain a pseudobolometric light curve from ~ 2000 to 24000 \AA with phase coverage from $t \approx -10.6$ to $+69.0$ days relative to B -band maximum. The result is presented in Appendix A.

We use the peak pseudobolometric luminosity to estimate the mass of ^{56}Ni synthesized in the explosion following Stritzinger & Leibundgut (2005),

$$L_{\max} = (6.34e^{-\frac{t_r}{8.8d}} + 1.45e^{-\frac{t_r}{111.3d}}) \frac{M_{\text{Ni}}}{M_{\odot}} \times 10^{43} \text{ erg s}^{-1}, \quad (2)$$

where t_r is the rise time of the pseudobolometric light curve. Using a fifth-order polynomial fit to the pseudobolometric light curve, we find a peak luminosity of $(1.71 \pm 0.24) \times 10^{43} \text{ erg s}^{-1}$ on MJD 60268.09 ± 0.08 and a rise time of $t_r^{\text{bolo}} = 16.44 \pm 0.09$ days. The pseudobolometric light curve peaks at about -1.35 days relative to the B -band maximum,

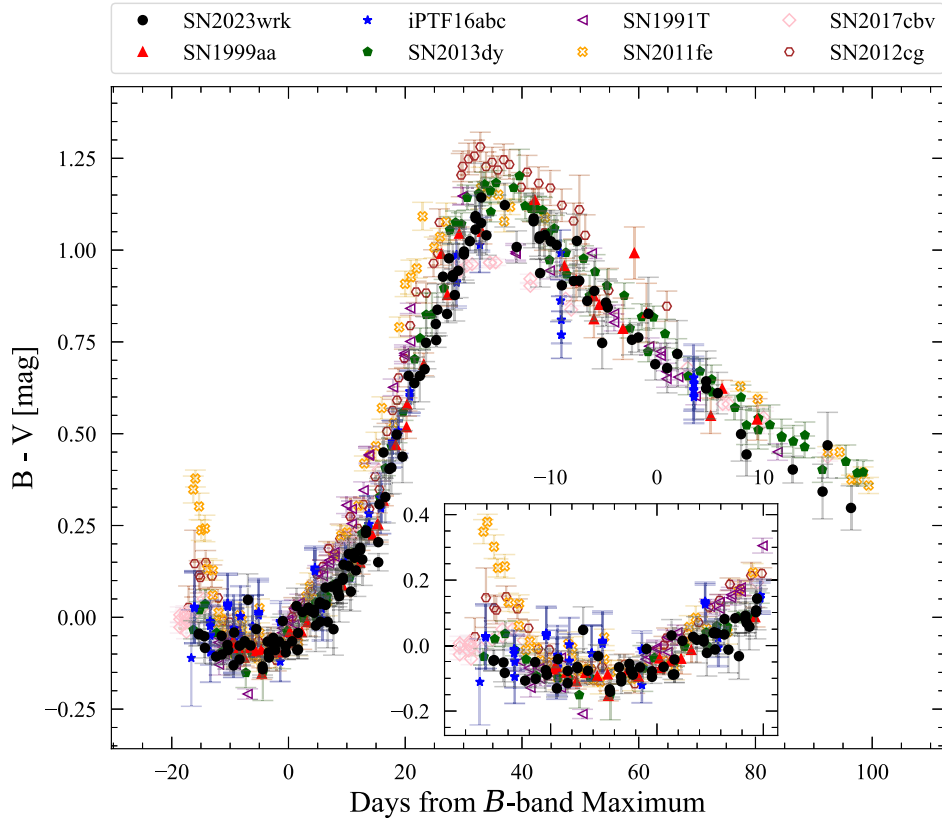


Figure 6. The $B - V$ color comparison between SN 2023wrk and SNe 1991T (Lira et al. 1998; Altavilla et al. 2004), 1999aa (Jha et al. 2006; Kowalski et al. 2008), 2011fe (Zhang et al. 2016), 2012cg (Stahl et al. 2019), 2013dy (Stahl et al. 2019), 2017cbv (Burns et al. 2020), and iPTF16abc (Miller et al. 2018). All of the color curves have been corrected for reddening due to the Milky Way and host galaxies. The inset shows the evolution during a phase from -20 to 10 days since B -band maximum light.

consistent with the statistical result from Scalzo et al. (2014) who give a mean difference of about -1 days. Then we derive a ^{56}Ni mass of $0.76 \pm 0.11 M_{\odot}$, which is in line with the ^{56}Ni mass of iPTF16abc ($0.76 M_{\odot}$) deduced by Aouad et al. (2024). In addition, we notice that the spectrum of SN 2023wrk is comparable with that of SN 2013dy and evidently more luminous than that of SN 2011fe around maximum light as shown in Figure 10.

5.2. Comparison of SN 2023wrk and Models

As presented and discussed in the previous sections, SN 2023wrk and iPTF16abc share extremely similar properties in both photometric and spectroscopic evolution, and can be considered twins of 99aa-like SNe Ia. In addition, both of these SNe Ia exploded at locations that are far from the center of their host galaxies, which may be related to galaxy mergers. The host of SN 2023wrk (NGC 3690) is a merging pair of galaxies, while the host of iPTF16abc (NGC 5221) has a long tidal tail that may arise from a galaxy merger. The above similarities suggest that these two SNe Ia may have the same physical origin.

Miller et al. (2018) performed comprehensive model comparisons for iPTF16abc. They found that the early-time light curve and color evolution of iPTF16abc can be best matched by the PDDEL models of Dessart et al. (2014) and the nickel-mixing models of Piro & Morozova (2016). The SN shock breakout and the companion interaction models are excluded by their early observations. They argued that either ejecta interaction with nearby unbound material or vigorous

mixing of ^{56}Ni to the outer region, or a combination of the two, can lead to the early-time characteristics of iPTF16abc. However, as Miller et al. (2018) noted, the PDDEL and nickel-mixing models need improvements to interpret the observations better.

5.2.1. Light-curve Comparison

Comparisons of the early light curve of SN 2023wrk and those predicted by some models are shown in Figure 11, where we assume that the time of first light and explosion are the same for SN 2023wrk, since this SN has nickel mixed in the outer layers. Note that a SN Ia could experience a dark phase lasting for a few days if its ^{56}Ni is confined to the innermost region (Piro & Nakar 2014). The B , g , and V light curves of SN 2023wrk are matched best by a PDDEL model with $\Delta m_{15}(B) = 0.95$ mag (PDDEL1) from $t \approx +4$ days after explosion to the peak, though the r -band light curve by PDDEL1 appears slightly brighter. The main defect is that PDDEL1 fails to match the luminosity bump of SN 2023wrk at $t \lesssim +4$ days. (i) The power-law index of the light curve of SN 2023wrk is broken at $t \approx +4$ days (see also Figure 4), which makes the light curve at $t \lesssim +4$ days look like a bump. However, such a transition in the light curve of PDDEL1 occurs at $t \approx +1$ days, indicating a much shorter duration for the bump than observed in SN 2023wrk. (ii) The PDDEL1 model is still too faint at $t \lesssim +4$ days, though it has extra radiation from the initial shock-deposited energy in the outer ejecta. Miller et al. (2018) mentioned that adding nickel mixing to the PDDEL models could reduce this inconsistency.

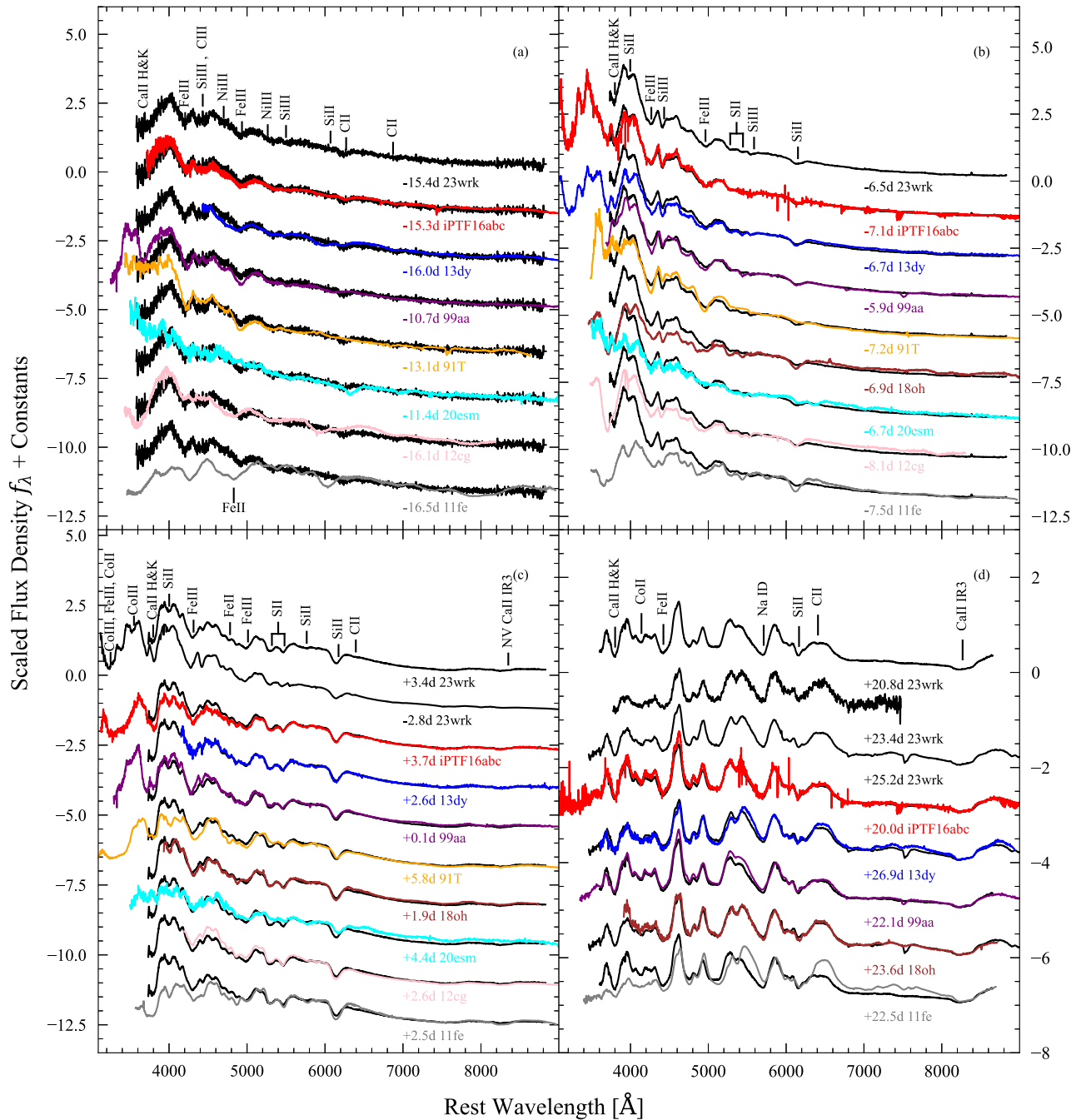


Figure 7. Spectral comparison of SN 2023wvk and SNe 1991T (Filippenko et al. 1992; Mazzali et al. 1995), 1999aa (Garavini et al. 2004; Kowalski et al. 2008; Matheson et al. 2008; Silverman et al. 2012), 2011fe (Mazzali et al. 2014; Zhang et al. 2016), 2012cg (Silverman et al. 2012; Marion & Brown 2016; Stahl et al. 2020), 2013dy (Zheng et al. 2013; Pan et al. 2015; Zhai et al. 2016), 2018oh (Li & Wang 2019; Yaron et al. 2023), 2020esm (Dimitriadis et al. 2022), and iPTF16abc (Miller et al. 2018) at several selected epochs ($t \approx -15, -7, +3,$ and $+20$ days relative to B -band maximum). The spectra have been corrected for reddening and host redshift.

Here we consider two mixing modes: (i) the extended mixing of Piro & Morozova (2016), which has a mass-fraction profile of ^{56}Ni monotonically decreasing toward the outer ejecta, and (ii) the ^{56}Ni -shell model of Magee & Maguire (2020), which has a high mass fraction of ^{56}Ni in the outer layers. We notice that the extended nickel-mixing model of Piro & Morozova (2016) does not produce a bump, while the ^{56}Ni -shell model of Magee & Maguire (2020) predicts a bump that breaks at $t \approx +4$ days after explosion. In fact, the light curve of SN 2023wvk matches best with the ^{56}Ni -shell model at $t \lesssim +4$ days.

The circumstellar matter (CSM) interaction model predicts a longer duration for the early excess emission compared with the

PDDEL1 model, but also a peak within a few days after explosion that is not seen in SN 2023wvk. A combination of CSM interaction and nickel mixing may improve the match. Specifically, the energy from the decay of the outward-mixing ^{56}Ni could prevent the flux from declining after the CSM interaction peak so that we would not see a peak within the first few days. In Figure 4, we compare the first 3 days light curve of SN 2023wvk with an extended nickel-mixing model P2016_mix_0.25, an ^{56}Ni -shell model M2020_17cbv_0.03_0.06, and a CSM + extended nickel-mixing model P2016_0.1CSM_1e11_0.15Ni, which has a boxcar averaging routine with a width $0.25 M_{\odot}$ and $0.1 M_{\odot}$ of CSM located at a radius of

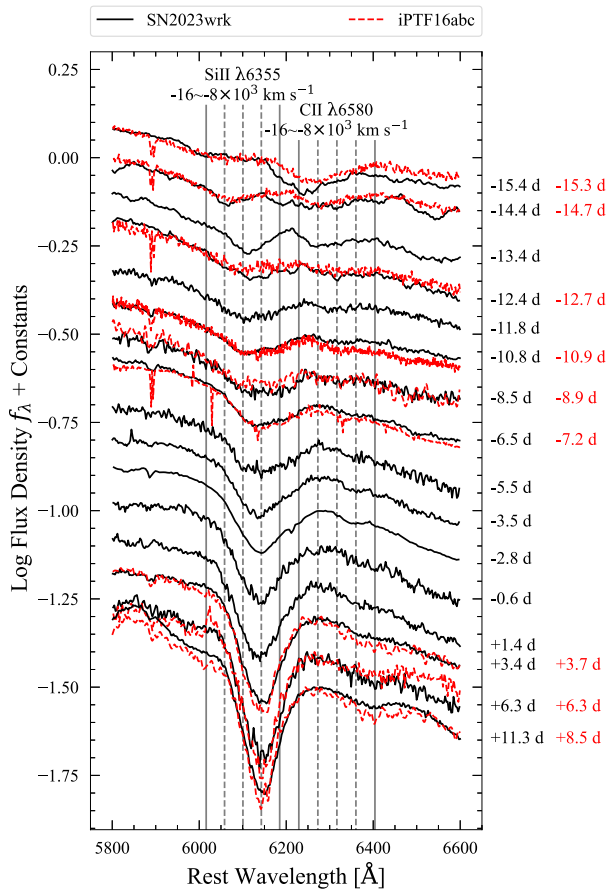


Figure 8. Evolution of the 5800–6600 Å region in spectra of SN 2023wrk and iPTF16abc, spanning phases from -15.4 to $+11.3$ days relative to B maximum. The spectra of SN 2023wrk at $t \approx -15.4$, -14.4 , and -13.4 days are smoothed with a Savitsky–Golay filter of order 1 and a window of 40 Å, and the spectrum at $t \approx -12.4$ days is smoothed with a window of 20 Å. All spectra have been corrected for reddening and host-galaxy redshift. The phase of each spectrum of SN 2023wrk is shown on the right side, and the phase of iPTF16abc is shown to the right of that of SN 2023wrk. The vertical lines mark the wavelength positions of Si II $\lambda 6355$ and C II $\lambda 6580$, corresponding to velocities from $-16,000$ to -8000 km s^{-1} with an interval of 2000 km s^{-1} . Spectra of SN 2023wrk and iPTF16abc are shown in black solid lines and red dashed lines, respectively.

10^{11} cm (Piro & Morozova 2016). The ^{56}Ni -shell model seems to have a nearly linear rise if we shift the time axis, but this shift means that the first-light time is ~ 0.3 days later than the explosion time, which conflicts with the observation of ^{56}Ni in the outer layers. The scaled flux yielded from the extended nickel-mixing model alone has a nonlinear rise, but that from the CSM + extended nickel-mixing model matches well with the observations of SN 2023wrk, though the scaled flux at $t \approx +1$ days is lower than the near-linear fit of SN 2023wrk. Some adjustments to the CSM + extended nickel-mixing model may better match the near-linear rise. Analogously, extra power from collision of ejecta and unbound material could also improve the ^{56}Ni -shell model.

5.2.2. Color Comparison

We compare the $B - V$ evolution between SN 2023wrk and some models in Figure 12. As Miller et al. (2018) mentioned, the extended nickel-mixing model is the only one that has a flat color evolution within days after explosion, though its $B - V$ color is ~ 0.1 mag redder than the observations. The ^{56}Ni -shell model matches the earliest point well, but its color tends to get redder in

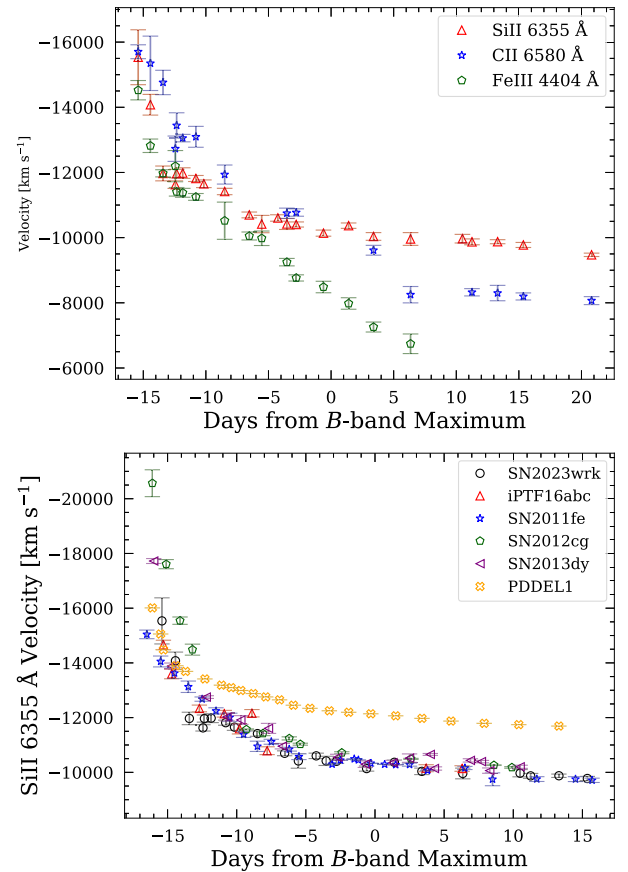


Figure 9. Top: evolution of velocity inferred from absorption minima of Si II $\lambda 6355$, C II $\lambda 6580$, and Fe II $\lambda 4404$ lines in SN 2023wrk. Bottom: comparison of Si II $\lambda 6355$ velocity evolution between SN 2023wrk and SNe 2011fe (Mazzali et al. 2014; Zhang et al. 2016), 2013dy (Zheng et al. 2013; Pan et al. 2015; Zhai et al. 2016), iPTF16abc (Miller et al. 2018), and the PDDEL1 model (Dessart et al. 2014).

Table 1
Parameters of SN 2023wrk

Parameter	Value
B_{\max}	14.08 ± 0.01 mag
$M_{\max}(B)$	-19.51 ± 0.15 mag
$E(B - V)_{\text{host}}$	0.028 ± 0.020 mag
$\Delta m_{15}(B)$	0.87 ± 0.02 mag
$t_{\max}(B)$	60269.45 ± 0.10 days
t_0	60251.48 ± 0.04 days
t_r^B	17.79 ± 0.11 days
t_r^{bol}	16.44 ± 0.09 days
L_{\max}^{bol}	$(1.71 \pm 0.24) \times 10^{43}$ erg s^{-1}
$M_{^{56}\text{Ni}}$	$0.76 \pm 0.11 M_{\odot}$
μ	33.42 ± 0.15 mag
$v_0(\text{Si II})$	$10, 100 \pm 100$ km s^{-1}
$\dot{v}(\text{Si II})$	31 ± 12 km s^{-1} day $^{-1}$

the following days. Meanwhile, PDDEL1 predicts a blue and flat color evolution from $t \approx +4$ to $+12$ days after explosion. It seems that a combination of the ^{56}Ni -shell and PDDEL1 models can match the observations better. At $t > 0$ day, the PDDEL1 model has a redder $B - V$ color than SN 2023wrk and thus a lower temperature. This can be seen clearly in the spectral comparison of SN 2023wrk and the PDDEL1 model near maximum light, where the spectrum of SN 2023wrk peaks at

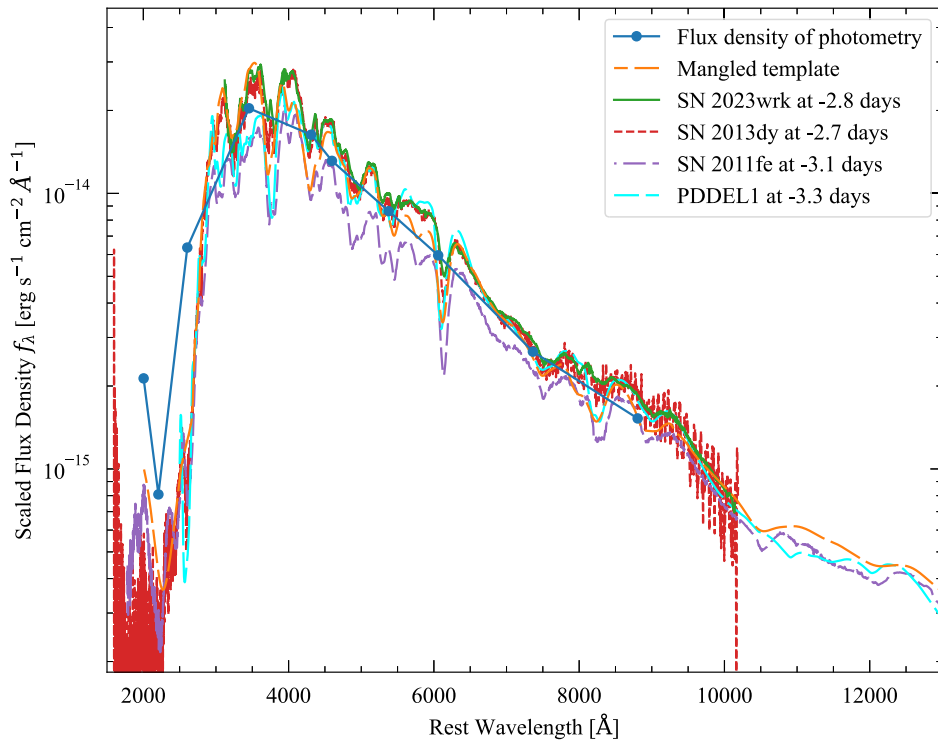


Figure 10. Comparison of the LRIS spectrum of SN 2023wrk and the synthetic spectrum of Hsiao et al. (2007) mangled by the photometry of SN 2023wrk at $t \approx -3$ days. Spectra of SN 2011fe (Mazzali et al. 2014) and SN 2013dy (Pan et al. 2015), and the synthetic spectrum of a PDDEL model (PDDEL1; Dessart et al. 2014) at similar epochs, are overplotted. All spectra have been corrected for reddening and host redshift. The flux density is scaled to the distance modulus of SN 2023wrk.

shorter wavelengths than that of PDDEL1 ($\sim 3500 \text{ \AA}$ versus $\sim 4000 \text{ \AA}$; see Figure 10). This could not be attributed to different total masses of ^{56}Ni , since the PDDEL1 model has a ^{56}Ni mass of $0.76 M_{\odot}$, which is close to that of SN 2023wrk.

The $B - V$ color of the CSM interaction model is very blue at first and then evolves redward quickly, which is seen in neither SN 2023wrk nor iPTF16abc. Nevertheless, it is still possible that the observation missed such evolution, and the color is quickly dominated by the outer ^{56}Ni . The one-dimensional standard delayed-detonation (DDT) model predicts a blueward color evolution within days after the explosion and thus is not consistent with SN 2023wrk, which could be improved by including the outward-mixing ^{56}Ni . Note that the collision of unbound carbon and SN ejecta in the PDDEL models is similar to the carbon-rich CSM interaction to some extent (Dessart et al. 2014), so including the CSM interaction in DDT models could also improve the match with observations.

5.2.3. Spectral Comparison

We compare the $t \approx -15$ days spectra of SN 2023wrk and some models in Figure 13. Little unburned carbon is left in a standard DDT model, so the DDC6 model spectrum at $t \approx -15.3$ days shows no evident carbon absorption trough. The PDDEL model retains more unburned carbon owing to the pulsation, and thus prominent carbon features are seen in the spectrum of PDDEL1. In fact, the C II $\lambda 6580$ lines of SN 2023wrk and PDDEL1 match well at $t \approx -15.4$ days. However, the PDDEL1 model has a clear Si II $\lambda 6355$ line that is nearly absent in SN 2023wrk. Aouad et al. (2024) find a silicon mass fraction of 0.013 at velocities $v > 13,450 \text{ km s}^{-1}$ for iPTF16abc, while the PDDEL1 model has a higher silicon mass fraction of ~ 0.35 in the same region. Thus, the weak silicon

features of iPTF16abc at $t \approx -15.3$ days can be attributed to silicon depletion in the outer layers. A similar case should hold for SN 2023wrk, as the spectra of these two SNe nearly overlap at this phase.

Note that the PDDEL1 model has a weaker Si II line than the DDC6 model, though their silicon mass fractions in line-forming regions are similar. This could be due to a spike structure in the density profile (called “cliff” by Dessart et al. 2014), caused by collision of SN ejecta with the unbound carbon in the PDDEL models, while this is absent in the DDC models. When the photosphere recedes to the cliff, the large density gradient of the cliff reduces the spatial extent of the line formation and thus produces weak lines (Dessart & Hillier 2005, 2005). This could explain the weak lines of SN 2023wrk.

The super- M_{Ch} model has a strong Si II $\lambda 6355$ line at $t \approx -15.4$ days, but this feature is nearly absent because the photosphere is formed in the swept-up envelope when including a carbon-rich CSM. Thus, the collision of SN ejecta with nearby carbon could make the photosphere form in a higher-velocity layer and partially cause the nearly absent Si II line of SN 2023wrk at very early phases. Thus, the presence of carbon-rich CSM can account for prominent carbon features in the spectrum. Note that the collision of SN ejecta and carbon-rich CSM can also lead to a cliff in the density profile.

Unlike the continuous receding in the DDC model, the photosphere of the PDDEL model resides within the cliff for a longer time because it represents a large jump in optical depth (Dessart et al. 2014). Notice that the Si II velocity of SN 2023wrk is observed to have a plateau near $\sim 12,000 \text{ km s}^{-1}$ during the period $t \approx -13.5$ to -8.5 days (see Figure 9), which may imply a cliff in density profile and thus supports a collision of SN ejecta and nearby material in SN 2023wrk. Moreover, it seems that such a cliff in SN 2023wrk is more prominent than that in

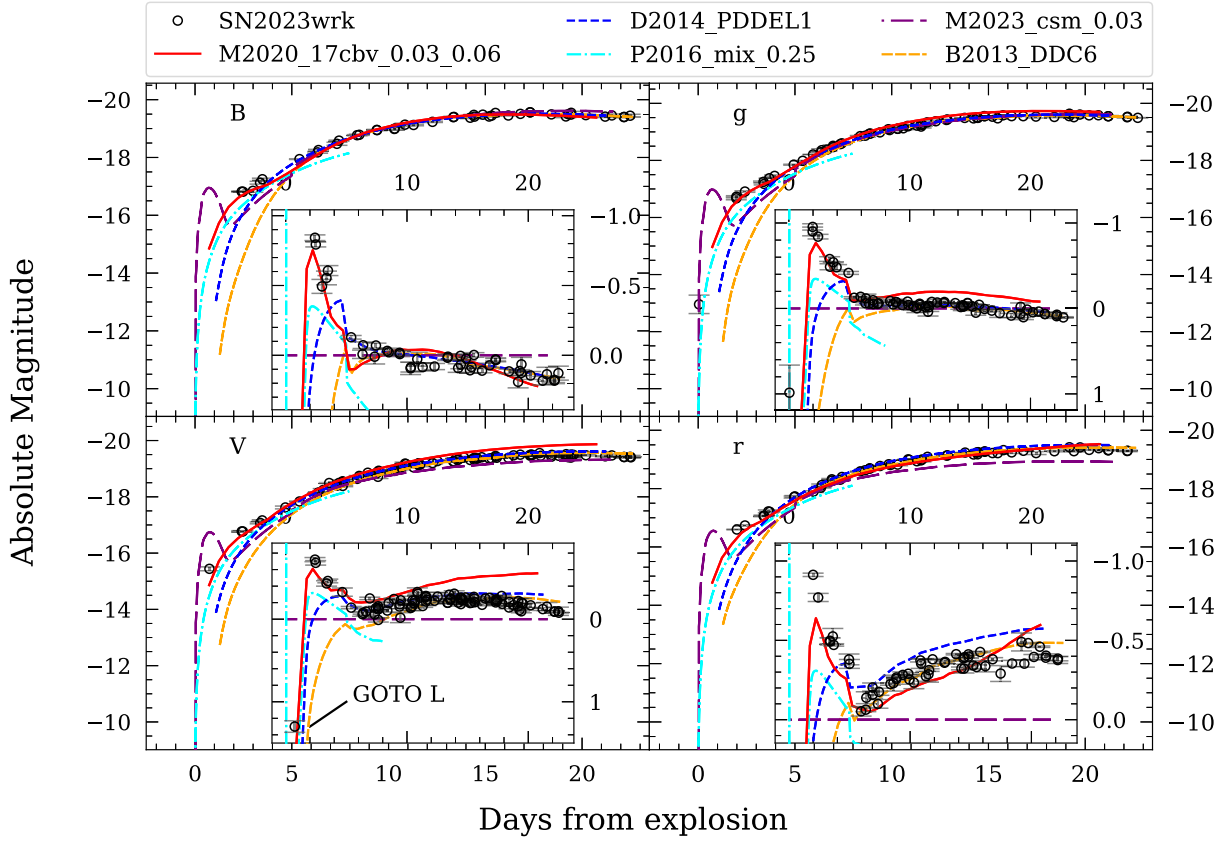


Figure 11. Comparison of early $BVgr$ -band light curves between SN 2023wrk and some models, including an extended nickel-mixing model of Piro & Morozova (2016), which uses a boxcar averaging routine with width $0.25 M_{\odot}$ (P2016_mix_0.25), a standard delayed-detonation model of Blondin et al. (2013) with $M_{56\text{Ni}} = 0.72 M_{\odot}$ (DDC6), an ^{56}Ni -shell model of Magee & Maguire (2020), which is based on their fiducial SN 2017cbv model and has an ^{56}Ni shell of $0.03 M_{\odot}$ with a width of $0.06 M_{\odot}$ (M2020_17cbv_0.03_0.06), a carbon-rich CSM interaction model of Maeda et al. (2023) based on a super-Chandrasekhar mass (super- M_{Ch}) explosion (M2023_csm_0.03), and a pulsational delayed-detonation model of Dessart et al. (2014) with $M_{56\text{Ni}} = 0.75 M_{\odot}$ (PDDEL1). The first detection by GOTO in the L band is plotted in the V -band subplot. The light curve of SN 2023wrk has been corrected for reddening. The insets show the residuals relative to the M2023_csm_0.03 model and the direct convolution of spectra ($t \gtrsim +5$ days; more realistic when interaction power is negligible).

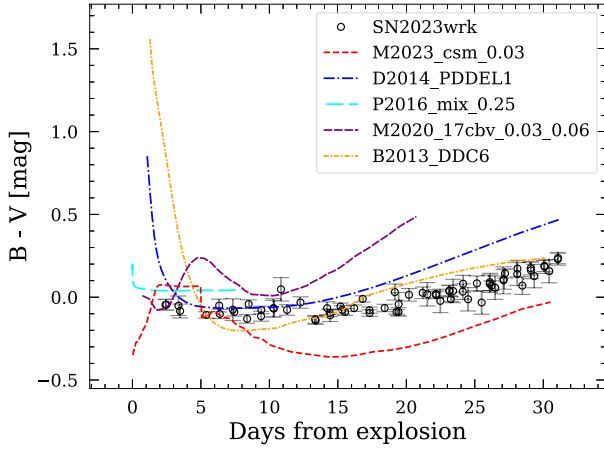


Figure 12. Comparison of early $B - V$ color between SN 2023wrk and the models presented in Figure 11. The $B - V$ color of SN 2023wrk has been corrected for reddening.

PDDEL1, as the Si II velocity of SN 2023wrk has a flatter plateau and a faster decline after the plateau.

In short, the PDDEL1 model gives a better match with SN 2023wrk, but some improvements are still needed. For instance, the luminosity is underestimated and the $B - V$ color is still too red at $t \lesssim +4$ days after explosion, which could be improved by including outward-mixing ^{56}Ni . In fact, the Ni III

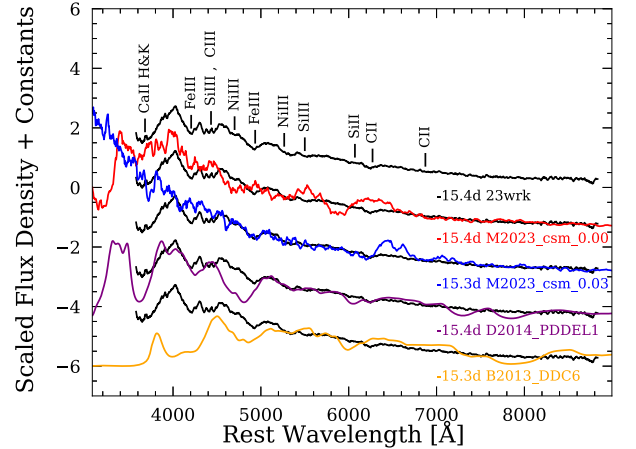


Figure 13. Spectral comparison between SN 2023wrk and synthetic spectra of some models at $t \approx -15$ days, including two super- M_{Ch} models without CSM interaction or with $0.03 M_{\odot}$ CSM interaction (M2023_csm_0.00 and M2023_csm_0.03; Maeda et al. 2023), an M_{Ch} delayed-detonation model (DDC6; Blondin et al. 2013), and an M_{Ch} pulsational delayed-detonation model (PDDEL1; Dessart et al. 2014). The spectrum of SN 2023wrk has been corrected for reddening and host redshift, and it has been smoothed with a window of 30 \AA .

features identified in the first spectrum of SN 2023wrk and the reappearance of carbon absorption around the time of B -band maximum light in an inner shell support the macroscopic mixing

of fuel and ash from multidimensional effects as predicted by the three-dimensional DDT model (Gamezo et al. 2005), in which the unburned carbon and oxygen mix inward and the intermediate-mass elements (IMEs) and iron-group elements (IGEs) mix outward when averaging over angle. As PDDEL1 has a larger silicon mass fraction than SN 2023wrk in the outer layers, this could also be improved by including outward-mixing IGEs. Note that, for the PDDEL models, an ^{56}Ni shell in the outer layer is needed to reproduce the bump in the early light curve, though it could also lead to a very red peak color that is inconsistent with SN 2023wrk. An alternative choice is the DDT model with a carbon-rich CSM. In this case, the bump in the light curve could be produced by combining CSM interaction and the radioactive decay of outward-mixing ^{56}Ni , and the blue and constant $B - V$ color evolution could arise from extended ^{56}Ni mixing.

5.3. Diversity among Carbon-rich SNe Ia

Besides iPTF16abc and SN 2023wrk, an increasing number of SNe Ia with strong C II $\lambda 6580$ absorption have been discovered, such as the normal objects SNe 2012cg, 2013dy, and 2017cbv, as well as 03fg-like or 02es-like SNe Ia. Here we call these objects “carbon-rich SNe Ia.” Besides the prominent carbon features, these SNe Ia show bluer colors and excess emission in optical and UV bands, and weaker Si II lines compared with the typical object SN 2011fe at early times. Except for 03fg-like or 02es-like objects, the light curves of carbon-rich SNe Ia are homogeneous around maximum light (see Figure 5), and we call them relatively normal carbon-rich SNe Ia. Nevertheless, significant diversity is still found among these carbon-rich SNe Ia. In this section, we briefly present this diversity and explore the possible origins.

In our comparison sample, SN 2023wrk and iPTF16abc are more similar to 91T/99aa-like objects, since they have very weak Si II and prominent Fe III lines, whereas SNe 2012cg, 2013dy, and 2017cbv are closer to normal SNe Ia, showing prominent Si II lines at early times. To measure the line-strength ratio of C II $\lambda 6580$ to Si II $\lambda 6355$, we determine the pseudoequivalent width (pEW) ratio of these two lines by performing two-component Gaussian fits to them normalized by a pseudocontinuum that is defined as a straight line connecting the interactively chosen points on the red and blue sides of each feature. We compare the pEW ratios of SN 2023wrk and some other SNe Ia with early-time observations in Figure 14; the individual pEW measurements as well as the values of the ratio can be found in Appendix D. As can be seen, the pEW ratio of C II $\lambda 6580$ to Si II $\lambda 6355$ is higher for the 03fg-like objects and the 02es-like objects, but is smaller for the normal SNe Ia and moderate for SN 2023wrk and iPTF16abc at comparable phases. If the unbound carbon is the main source of the strong carbon features, the diversity of the line-strength ratio may partially stem from different properties of the unbound carbon. For instance, more massive unbound carbon could lead to stronger and longer-lasting carbon features and probably weaker silicon lines owing to the formation of the photosphere above more of the silicon. Another difference is the early $B - V$ color evolution: it takes a longer time for SNe 2012cg, 2013dy, and 2017cbv to evolve to the blue, while SN 2023wrk and iPTF16abc have a constant $B - V$ color before maximum light. This may be due to different properties of the outward-mixing ^{56}Ni , since a higher mass fraction of ^{56}Ni in the outer layers can shorten the time to evolve blueward (see Figure 8 of Piro & Morozova 2016). In

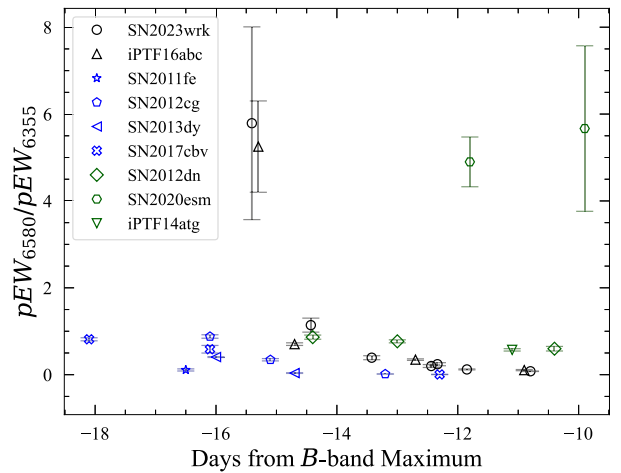


Figure 14. Comparison of evolution of the pEW ratio of C II $\lambda 6580$ to Si II $\lambda 6355$ in SN 2023wrk and SNe 2011fe, 2012cg, 2013dy, 2017cbv (Hosseinza-deh et al. 2017), 2012dn (Parrent et al. 2016; Stahl et al. 2020), 2020esm (Dimitriadis et al. 2022), iPTF14atg (Cao et al. 2015), and iPTF16abc. 91T/99aa-like SNe Ia are shown in black, normal SNe Ia are in blue, and 03fg-like or 02es-like objects are in dark green. The references for spectra of SNe 2011fe, 2012cg, 2013dy, and iPTF16abc can be found in the caption of Figure 9.

addition, it could explain the higher Fe III/Fe II ratios in the early spectra of SN 2023wrk and iPTF16abc.

Most of the 03fg-like or 02es-like SNe Ia are more peculiar than other carbon-rich SNe Ia and deviate from the Phillips relation (Figure 1 of Taubenberger 2017). Hoogendam et al. (2024) find that these objects have much bluer UV–optical colors than other SNe Ia, which indicates little line blanketing by IGEs and thus probably little outward-mixing IGEs. These peculiar properties imply that different explosion mechanisms may exist in these objects and other carbon-rich SNe Ia. For example, the violent merger (e.g., Pakmor et al. 2012) of two C/O WDs is a popular model to explain the 03fg-like objects (e.g., SN 2022pul; Siebert et al. 2024), where a detonation is triggered during the merger. Thus, in contrast to the three-dimensional DDT model, there are no outward-mixing IGEs through a deflagration in the violent merger.

There is also diversity among normal carbon-rich SNe Ia. Within the first few days after explosion, SN 2013dy and SN 2017cbv are more luminous and slightly bluer than SN 2012cg, and their Si II $\lambda 6355$ velocity is smaller than that of SN 2012cg. The pEW ratios of C II $\lambda 6580$ to Si II $\lambda 6355$ of these three SNe Ia are similar at $t \approx -16$ days. But as seen in Figure 7, the C II $\lambda 6580$ and Si II $\lambda 6355$ line profiles of SN 2012cg and SN 2013dy are also different. For instance, the absorption minimum of C II $\lambda 6580$ has a smaller optical depth than that of Si II $\lambda 6355$ in SN 2012cg, while the minima of these two lines have a similar optical depth in SN 2013dy. Also, the P Cygni emission around 6500 \AA in SN 2012cg is stronger than that in SN 2013dy. Instead of the simple two-component Gaussian fits, more detailed analysis of the features is needed to accurately examine the difference. In addition, another normal object (SN 2018oh) is potentially a carbon-rich SN Ia, since its C II $\lambda 6580$ line at $t \approx -8.5$ days is still evident (Li & Wang 2019). Different from SNe 2012cg, 2013dy, and 2017cbv, the carbon features of SN 2018oh reappeared after B -band maximum. This difference could be attributed to a viewing-angle effect if the inner carbon comes from asymmetric macroscopic mixing

during the deflagration stage. But how the inner carbon survives in the subsequent detonation still needs to be explained.

It is important to study the progenitor system and explosion mechanism of the relatively normal carbon-rich SNe Ia such as SN 2023wrk and SN 2013dy, since they could be used as standardizable candles and are usually more luminous than other normal SNe Ia such as SN 2011fe. The diversity of the luminosity, color evolution, and absorption lines at very early times and the similarities around maximum light provide some clues for understanding their connections. However, the current sample of carbon-rich SNe Ia is very limited, and many more carbon-rich SNe Ia are needed to further explore their origins

6. Conclusion

In this paper, we present extensive photometric and spectroscopic observations of SN 2023wrk. It shows very close resemblances to iPTF16abc in many respects, including (1) evolution of early excess emission, (2) prominent but short-lived C II $\lambda 6580$ absorption at early times and the reappearance from maximum light to three weeks thereafter, (3) a blue, constant $B - V$ color before maximum light, and (4) a location far away from the center of the host galaxy. After careful comparison with models, the early light-curve bump and the blue $B - V$ color seen in SN 2023wrk are found to be more consistent with the outer ^{56}Ni -shell model proposed by Magee & Maguire (2020). The subsequent evolution seems to be better matched by the PDDEL1 model (Dessart et al. 2014), though this model yields a redder SED around maximum light. The Ni III lines detected in very early spectra and the appearance of C II lines in postpeak spectra indicate macroscopic mixing of fuel and ash, as a result of multidimensional effects predicted by the three-dimensional DDT model. The ^{56}Ni mixing alone cannot explain the early linear rise in flux, which may be improved by including energy from the collision of SN ejecta with nearby material such as the unbound carbon in a CSM or PDDEL model. The carbon collision is supported by the strong carbon features in very early spectra and the $\sim 12,000 \text{ km s}^{-1}$ plateau seen in the Si II $\lambda 6355$ velocity evolution. A combination of a carbon-rich CSM and an M_{Ch} DDT model with strong ^{56}Ni mixing may be an attractive model to interpret all the observations of SN 2023wrk; it needs to be explored in future work.

We find some diversity among carbon-rich SNe Ia that have comparable C II $\lambda 6580$ and Si II $\lambda 6355$ lines in very early spectra, including the line-strength ratio of C II $\lambda 6580$ to Si II $\lambda 6355$, the iron absorption profile, the early-time luminosity, and the color evolution. Differences in properties of unbound carbon and outward-mixing ^{56}Ni could partially account for this diversity. More carbon-rich SNe Ia with very early observations are needed to further explore their connections and origins.

Acknowledgments

This work is supported by the National Natural Science Foundation of China (NSFC grants 12288102, 12033003, and 12090044) and the Tencent Xplorer Prize. J.Z.L. is supported by the Tianshan Talent Training Program through grant 2023TSYCCX0101. J.-J.Z. and Y.-Z.C. are supported by the International Centre of Supernovae, Yunnan Key Laboratory (No. 202302AN360001). J.-J.Z. is supported by the National Key R&D Program of China (No. 2021YFA1600404), NSFC grant 12173082, the Yunnan Province Foundation (grant 202201AT070069), the Top-notch Young Talents Program of

Yunnan Province, and the Light of West China Program provided by the Chinese Academy of Sciences. Y.-Z.C. is supported by NSFC grant 12303054 and Yunnan Fundamental Research Projects grant 202401AU070063. A.V.F.’s group at UC Berkeley received financial assistance from the Christopher R. Redlich Fund, as well as donations from Gary and Cynthia Bengier, Clark and Sharon Winslow, Alan Eustace, William Draper, Timothy and Melissa Draper, Briggs and Kathleen Wood, and Sanford Robertson (W.Z. is a Bengier–Winslow–Eustace Specialist in Astronomy, T.G.B. is a Draper–Wood–Robertson Specialist in Astronomy, Y.Y. was a Bengier–Winslow–Robertson Fellow in Astronomy), and numerous other donors. X.L. is supported by the Innovation Project of Being Academy of Science and Technology (24CD013). A.R. acknowledges financial support from the GRAWITA Large Program Grant (PI P. D’Avanzo) and the PRIN-INAF 2022 program “Shedding light on the nature of gap transients: from the observations to the models.” I.M. is grateful for support from Severo Ochoa grant CEX2021-001131-S funded by MCIN/AEI/ 10.13039/501100011033.

The work of F.N. is supported by NOIRLab, which is managed by the Association of Universities for Research in Astronomy (AURA) under a cooperative agreement with the National Science Foundation. W. Corradi is supported by Laboratório Nacional de Astrofísica (LNA) through project numbers P-003, P-011, I-004, and I-013 from OPD. The work of L. de Almeida is supported by Laboratório Nacional de Astrofísica (LNA) through project numbers I-009, I-022, I-027, and P-008 from OPD. N. Sasaki is supported by Universidade do Estado do Amazonas—UEA and LNA through project numbers P-003, P-008, I-004, and I-007. This work is supported by CNRS-MITI and Programme National des Hautes Energies (PNHE).

We thank the staffs at the various observatories where data were obtained. A major upgrade of the Kast spectrograph on the Shane 3 m telescope at Lick Observatory, led by Brad Holden, was made possible through generous gifts from the Heising-Simons Foundation, William and Marina Kast, and the University of California Observatories. Research at Lick Observatory is partially supported by a generous gift from Google. Some of the data presented herein were obtained at the W. M. Keck Observatory, which is operated as a scientific partnership among the California Institute of Technology, the University of California, and NASA; the observatory was made possible by the generous financial support of the W. M. Keck Foundation. The data presented here were obtained in part with ALFOSC, which is provided by the Instituto de Astrofísica de Andalucía (IAA-CSIC) under a joint agreement with the University of Copenhagen and NOT. This work is partially based on observations collected with the Copernico 1.82 m telescope and the Schmidt 67/92 telescope (Asiago Mount Ekar, Italy) of the INAF—Osservatorio Astronomico di Padova. We thank Stefan Taubenberger and his group of students from MPA for an epoch of ALFOSC imaging and a spectrum taken during a run for educational observations at the 1.82 m Copernico telescope. Part of the photometric data of this work were obtained by the Nanshan One-meter Wide-field Telescope, which is supported by Tianshan Talent Training Program (grant 2023TSYCLJ0053) and the National Key R&D program of China for Intergovernmental Scientific and Technological Innovation Cooperation Project under grant 2022YFE0126200. We acknowledge the support of the staff of the Xinglong 80 cm telescope (TNT). This work was partially

supported by the Open Project Program of the Key Laboratory of Optical Astronomy, National Astronomical Observatories, Chinese Academy of Sciences. This research was partially based on observations made with the Thai Robotic Telescope under program ID TRTToO_2024001 and TRTC11B_002, which is operated by the National Astronomical Research Institute of Thailand (Public Organization). The ZTF forced-photometry service was funded under Heising-Simons Foundation grant 12540303 (PI M. Graham). This work makes use of the NASA/IPAC Extragalactic Database (NED), which is funded by NASA and operated by the California Institute of Technology.

This article is based in part on observations made at the Observatorios de Canarias del IAC with the TNG telescope operated on the island of La Palma by the Fundación Galileo Galilei INAF, Fundación Canaria (FGG), in the Observatorio del Roque de los Muchachos (ORM). The operation of FRAM telescopes is supported by grants of the Ministry of Education of the Czech Republic LM2023032 and LM2023047, as well as EU/MEYS grants CZ.02.1.01/0.0/0.0/16_013/0001403, CZ.02.1.01/0.0/0.0/18_046/0016007, CZ.02.1.01/0.0/0.0/16_019/0000754, and CZ.02.01.01/00/22_008/0004632. NRIAG team acknowledges financial support from the Egyptian Science, Technology & Innovation Funding Authority (STDF) under grant number 45779. Based in part on observations made at Observatoire de Haute Provence (CNRS), France, with the MISTRAL instrument. This research has also made use of the MISTRAL database, operated at CeSAM (LAM), Marseille, France. We acknowledge the excellent support from Observatoire de Haute-Provence, in particular Jerome Schmitt, Jean Claude Brunel, Francois Huppert, Jean Balcaen, Yoann Degot-Longhi, Stephane Favard, and Jean-Pierre Troncin. We thank the OHP director for the allocations of two DDT observing slots. The work of K. Noysena and M. Tanasan is based on observations made with the Thai Robotic Telescope under program ID TRTC11A_003, which is operated by the National Astronomical Research Institute of Thailand (Public Organization). We acknowledge resources at IJCLAB for hosting science portals and data-reduction pipelines thanks to J. Peloton.

We acknowledge major contributions from the GRANDMA Collaboration and the Kilonova-Catcher citizen science program for the photometric and spectroscopic observations taken over 3 months and their subsequent data reduction. The authors express special gratitude to the PI of GRANDMA and the core team who decided to allocate substantial resources of the collaboration to the study of SN 2023wrk (S. Antier, D. Turpin, I. Tosta e Melo, M. Coughlin, P. Hello, P.-A. Duverne, S. Karpov, T. Pradier, J. Peloton, A. Klotz, C. Andrade). We thank observers of the GRANDMA network program who actively participated in the follow-up campaign: AbAO observatory (N. Kochiashvili, R. Inasaridze and V. Aivazyan) for 1 observation; ShAO Observatory (N. Ismailov, Z. Vidadi, S. Aghayeva, S. Alishov, E. Hesenov) for 3 observations; HAO telescopes (A. Kaeouach) for 12 observations; FRAM telescopes (M. Mašek and S. Karpov) for 194 observations; KAO telescope (E. G. Elhosseiny, M. Abdelkareem, A. Takey, R. H. Mabrouk, A. Shokry, M. Aboueisha, Y. Hendy, A. E. Abdelaziz, R. Bendary, I. Zead, T. M. Kamel, G. M. Hamed, S. A. Ata, W. A. Badawy) for 67 observations; TRT (K. Noysena, M. Tanasan) for 3 observations; and TBC, UBAI telescopes (Y. Tillayev, O. Burkhonov, Sh. Ehgamberdiev, Y. Rajabov) for 9 observations. We acknowledge operations within GRANDMA with crucial participation of 22

follow-up advocates (C. Andrade, P. Gokuldass, M. Tanasan, I. Abdi, D. Akl, P. Hello, O. Pyshna, A. Simon, J.-G. Ducoin, Y. Tillayev, M. Mašek, Z. Vidadi, Y. Rajabov, S. Antier, T. Leandro de Almeida, F. Navarete, N. Sasaki, W. Corradi, I. Tosta e Melo, M. Coughlin, T. Hussenot-Desenonges, S. Aghayeva) and their leaders (C. Andrade, P. Hello, S. Antier, I. Tosta e Melo), who participated in providing adequate observation strategies. We thank the whole Data Analysis Group of GRANDMA consisting of I. Abdi, D. Akl, C. Andrade, J.-G. Ducoin, P.-A. Duverne, S. Karpov, F. Navarete, and D. Turpin. P.-A. Duverne is grateful to Etienne Bertrand and Emmanuel Soubrouillard for providing the source's spectra and their help in analyzing these data. D. Turpin, PI of the Kilonova-Catcher, acknowledges the observers of the Kilonova-Catcher program who actively participated in the follow-up campaign: E. Broens, F. Dubois, M. Freeberg, C. Galdies, R. Kneip, D. Marchais, E. Maris, R. Ménard, M. Odeh, G. Parent, A. Popowicz, D. ST-Gelais, and M. Serrau. We also thank Unistellar observers B. Guillet, B. Haremza, G. Di Tommaso, K. Borrot, M. Lorber, M. Shimizu, M. Mitchell, N. Meneghelli, N. Delaunoy, O. Clerget, P. Huth, P. Heafner, P. Kuossari, S. Saibi, S. Price, W. Ono, and Y. Arnaud.

Software: AUTOPHOT (Brennan & Fraser 2022), HEASOFT (<https://www.swift.ac.uk/analysis/software.php>), Matplotlib (Hunter 2007), NumPy (Harris et al. 2020), Pandas (<http://pandas.pydata.org/>), SciPy (Virtanen et al. 2020), SNooPy2 (Burns et al. 2011), STDPipe (Karpov 2021).

Appendix A Photometric and Pseudobolometric Light Curves

A summary of photometric observations triggered by us is presented in Table 2, including telescope names and the corresponding filters and number of images. The full photometric data of SN 2023wrk are presented in Table 3. The estimated pseudobolometric light curve is presented in Table 4.

Table 2
Summary of Photometric Observations

Facility	Number of Images	Bands
Atlas Sky Observatory (ASO)	8	<i>L, g, r, i</i>
Abastumani-T70	1	<i>R</i>
FRAM-CTA-N	194	<i>B, V, R</i>
HAO	8	<i>R, V, g</i>
KAO	67	<i>g, r, i, z</i>
Lisnyky-Schmidt-Cassegrain	1	<i>R</i>
ShAO-2 m	3	<i>B, V, R</i>
TRT-SRO	3	<i>B, V</i>
UBAI-NT60	6	<i>B, V, R</i>
UBAI-ST60	3	<i>B, V, R</i>
Kilonova-Catcher (17 amateur telescopes)	337	<i>B, V, R, I, g, r, i</i>
Copernico	20	<i>B, V, u, g, r, i, z</i>
LJT	48	<i>B, V, g, r, i, z</i>
NOWT	102	<i>U, B, V, R, I</i>
TNT	387	<i>B, V, g, r, i</i>
67/91-ST	52	<i>B, V, u, g, r, i</i>

Table 3
Observed Photometry of SN 2023wrk

MJD	Magnitude	Error ^a	Band	Source
60251.524	20.621	0.323	<i>g</i>	ZTF
60252.229	18.110	0.070	<i>L</i>	GOTO
60253.467	16.905	0.051	<i>g</i>	ZTF
60253.470	16.850	0.037	<i>g</i>	ZTF
60253.497	16.930	0.011	<i>r</i>	ZTF
60253.915	16.777	0.020	<i>B</i>	LJT
60253.917	16.780	0.025	<i>V</i>	LJT
60253.918	16.668	0.027	<i>g</i>	LJT
60253.920	16.792	0.026	<i>r</i>	LJT
60253.922	17.072	0.039	<i>i</i>	LJT
60253.971	16.683	0.040	<i>I</i>	NOWT
...
60366.826	17.835	0.045	<i>B</i>	NOWT
60366.830	17.495	0.040	<i>V</i>	NOWT
60366.834	17.549	0.027	<i>R</i>	NOWT
60366.839	17.677	0.059	<i>I</i>	NOWT

Note.^a 1σ .(This table is available in its entirety in machine-readable form in the [online article](#).)

Table 4
Estimated Bolometric Light Curve of SN 2023wrk

Phase ^a (day)	L (10^{42} erg s ⁻¹)	Error ^b (10^{42} erg s ⁻¹)	Phase (day)	L (10^{42} erg s ⁻¹)	Error (10^{42} erg s ⁻¹)	Phase (day)	L (10^{42} erg s ⁻¹)	Error (10^{42} erg s ⁻¹)
-10.592	7.203	0.195	16.921	6.368	0.172	44.635	2.237	0.095
-9.712	8.698	0.216	17.746	6.105	0.158	45.544	2.152	0.093
-8.744	10.347	0.240	18.476	5.896	0.149	46.821	2.044	0.091
-7.714	12.039	0.264	19.728	5.584	0.139	47.121	2.020	0.090
-6.738	13.480	0.288	20.895	5.343	0.134	48.443	1.924	0.088
-6.042	14.393	0.309	21.650	5.200	0.133	49.709	1.844	0.086
-4.768	15.721	0.351	22.823	5.007	0.134	50.779	1.784	0.083
-3.802	16.424	0.383	23.537	4.900	0.135	51.202	1.759	0.082
-3.052	16.784	0.412	24.855	4.716	0.140	52.446	1.699	0.079
-1.973	17.031	0.461	25.453	4.639	0.144	53.741	1.644	0.074
-0.703	16.956	0.516	26.764	4.472	0.153	54.444	1.617	0.071
-0.272	16.853	0.528	27.884	4.332	0.162	55.279	1.588	0.068
1.106	16.318	0.521	28.695	4.231	0.167	56.531	1.547	0.065
1.942	15.870	0.482	29.963	4.074	0.172	57.394	1.520	0.064
3.252	15.038	0.408	30.658	3.988	0.171	58.771	1.478	0.064
4.184	14.380	0.374	31.961	3.824	0.164	59.362	1.460	0.065
5.202	13.624	0.349	32.831	3.714	0.156	60.212	1.433	0.066
6.041	12.981	0.324	33.909	3.575	0.145	61.645	1.385	0.067
7.053	12.205	0.284	34.418	3.509	0.140	62.453	1.355	0.067
8.177	11.343	0.241	35.635	3.349	0.128	63.562	1.311	0.067
9.128	10.631	0.220	36.827	3.189	0.119	64.493	1.281	0.070
10.123	9.915	0.218	37.488	3.100	0.114	65.591	1.229	0.068
11.094	9.258	0.226	38.849	2.918	0.108	66.506	1.182	0.065
12.047	8.659	0.234	39.640	2.814	0.105	67.560	1.123	0.061
13.139	8.031	0.235	40.620	2.689	0.103	68.098	1.091	0.058
13.924	7.624	0.228	41.716	2.555	0.100	68.960	1.037	0.052
15.377	6.956	0.204	42.744	2.436	0.098
15.855	6.762	0.194	43.815	2.320	0.096

Notes.^a Relative to *B*-band maximum, $\text{MJD}_{B\text{max}} = 60269.45$.^b Uncertainty in the distance not included. 1σ .(This table is available in machine-readable form in the [online article](#).)

Appendix B Spectroscopic Observations

The journal of spectroscopic observations of SN 2023wrk is presented in Table 5.

Table 5
Overview of Optical Spectra of SN 2023wrk

MJD	Date	Phase ^a	Range (Å)	Exposure (s)	Instrument/Telescope
60253.9	20231105	−15.4	3616–8925	2201	YFOSC/LJT
60254.9	20231106	−14.4	3772–8917	2700	BFOSC/XLT
60255.9	20231107	−13.4	3523–8925	2200	YFOSC/LJT
60256.9	20231108	−12.4	3518–8926	2200	YFOSC/LJT
60257.0	20231108	−12.3	3704–8182	300	AFOSC/Copernico
60257.5	20231109	−11.8	3636–10732	1800	Kast/Shane
60258.5	20231110	−10.8	3636–10734	1800	Kast/Shane
60259.2	20231111	−10.2	4111–8119	2700	MISTRAL/OHP
60260.9	20231112	−8.5	3769–8918	3000	BFOSC/XLT
60262.9	20231114	−6.5	3772–8919	3600	BFOSC/XLT
60263.9	20231115	−5.5	3772–8919	2400	BFOSC/XLT
60265.2	20231117	−4.2	4090–8062	4200	MISTRAL/OHP
60265.9	20231117	−3.5	3771–8918	2400	BFOSC/XLT
60266.6	20231118	−2.8	3152–10251	180	LRIS/Keck I
60268.3	20231120	−1.2	4003–7867	300	DOLoRES-LRS/TNG
60268.8	20231120	−0.6	3777–8915	1800	BFOSC/XLT
60270.9	20231122	1.4	3775–8914	2400	BFOSC/XLT
60272.9	20231124	3.4	3772–8919	2700	BFOSC/XLT
60275.9	20231127	6.3	3775–8917	3000	BFOSC/XLT
60280.1	20231202	10.5	3926–7437	10800	EBE
60280.8	20231202	11.3	3774–8915	3000	BFOSC/XLT
60282.9	20231204	13.3	3774–8915	3000	BFOSC/XLT
60285.0	20231206	15.4	3389–9283	900	AFOSC/Copernico
60290.5	20231212	20.8	3640–8745	2100	HIRES/Shane
60293.1	20231215	23.4	3816–7551	7200	ESOU
60295.0	20231216	25.2	3501–9278	900	AFOSC/Copernico
60295.0	20231216	25.3	4093–7434	7200	EBE
60296.8	20231218	27.1	3777–8916	3600	BFOSC/XLT
60313.9	20240104	44.0	3614–8925	1800	YFOSC/LJT
60314.9	20240105	44.9	3775–8915	3000	BFOSC/XLT
60316.0	20240106	46.0	3942–7444	10800	EBE
60320.9	20240111	50.9	3996–7420	14400	EBE
60321.4	20240112	51.4	3638–10756	1200	Kast/Shane
60321.4	20240112	51.4	3637–8731	3600	HIRES/Shane
60329.0	20240119	58.9	3988–7443	14400	EBE
60330.0	20240121	60.0	3900–7200	7200	ESOU
60332.1	20240123	62.0	4300–8121	2700	MISTRAL/OHP
60380.3	20240311	109.7	3622–10754	3000	Kast/Shane

Note.

^a Relative to the *B*-band maximum light, $\text{MJD}_{B_{\text{max}}} = 60269.45$.

(This table is available in machine-readable form in the [online article](#).)

Appendix C Parameters of Comparison SNe Ia in this Work

The adopted distance modulus, total reddening, time of first light, and the references of the comparison SNe Ia in this work are presented in Table 6.

Table 6
Parameters and References of the Comparison SNe Ia

Name	μ^a (mag)	$E(B - V)$ (mag)	t_0^b	Early Excess?	References
SN 2011fe	29.04 ± 0.08	0.04	55796.84	No	(1, 2, 3)
SN 2012cg	30.91 ± 0.30	0.2	56062.7	Yes	(2, 4, 5)
SN 2013dy	31.50 ± 0.08	0.3	56482.99	Yes	(2, 6, 7)
SN 2017cbv	30.58 ± 0.05	0.145	57821.9	Yes	(2,8,9)
SN 2018oh	33.61 ± 0.05	0.038	58144.3	Yes	(2, 10, 11, 12)
iPTF16abc	35.08 ± 0.15	0.078	57481.21	Yes	(2, 13, 14, 15)

Notes.

^a Distance modulus.

^b Time of first light (MJD).

References: (1) Macri et al. (2001); (2) Schlafly & Finkbeiner (2011); (3) Zhang et al. (2016); (4) Cortés et al. (2008); (5) Silverman et al. (2012); (6) Riess et al. (2016); (7) Zheng et al. (2013); (8) Wang et al. (2020); (9) Hosseinzadeh et al. (2017); (10) Li & Wang (2019); (11) Shappee et al. (2019); (12) Dimitriadis et al. (2019); (13) Mould et al. (2000); (14) Ferretti et al. (2017); (15) Miller et al. (2018).

Appendix D Results of pEW Measurements

The pEWs of C II $\lambda 6580$ and Si II $\lambda 6355$ measured by the two-component Gaussian fits as well as their ratios are presented in Table 7.

Table 7
Individual pEWs Measurements as well as the Values of the Ratio

Name	Phase (day)	pEW(C II 6580 Å) (Å)	pEW(Si II 6355 Å) (Å)	pEW(C II 6580 Å)/pEW (Si II 6355 Å)
SN 2023wrk	-15.4	22.17 ± 1.37	3.83 ± 1.45	5.79 ± 2.22
SN 2023wrk	-14.4	17.34 ± 1.64	15.20 ± 1.60	1.14 ± 0.16
SN 2023wrk	-13.4	10.68 ± 1.16	27.29 ± 1.26	0.39 ± 0.05
SN 2023wrk	-12.4	6.51 ± 0.93	32.65 ± 2.92	0.20 ± 0.03
SN 2023wrk	-12.3	7.33 ± 1.00	30.39 ± 1.55	0.24 ± 0.04
SN 2023wrk	-11.8	3.73 ± 0.29	30.79 ± 1.08	0.12 ± 0.01
SN 2023wrk	-10.8	2.30 ± 0.16	29.10 ± 0.56	0.08 ± 0.01
iPTF16abc	-15.3	18.85 ± 0.56	3.59 ± 0.71	5.25 ± 1.05
iPTF16abc	-14.7	13.14 ± 0.37	18.67 ± 0.60	0.70 ± 0.03
iPTF16abc	-12.7	8.99 ± 0.35	25.92 ± 0.82	0.35 ± 0.02
iPTF16abc	-10.9	3.30 ± 0.41	31.32 ± 0.82	0.11 ± 0.01
SN 2011fe	-16.5	11.97 ± 2.56	109.47 ± 6.28	0.11 ± 0.02
SN 2012cg	-16.1	59.97 ± 1.97	68.20 ± 2.14	0.88 ± 0.04
SN 2012cg	-15.1	35.73 ± 2.56	103.82 ± 3.01	0.34 ± 0.03
SN 2012cg	-13.2	1.68 ± 0.49	102.99 ± 1.28	0.02 ± 0.00

Table 7
(Continued)

Name	Phase (day)	pEW(C II 6580 Å) (Å)	pEW(Si II 6355 Å) (Å)	pEW(C II 6580 Å)/pEW (Si II 6355 Å)
SN 2013dy	-16.0	28.53 ± 0.52	70.20 ± 1.16	0.41 ± 0.01
SN 2013dy	-14.7	3.13 ± 0.72	82.92 ± 1.80	0.04 ± 0.01
SN 2017cbv	-18.1	43.47 ± 1.34	53.33 ± 1.59	0.82 ± 0.04
SN 2017cbv	-16.1	34.97 ± 4.58	59.69 ± 4.26	0.59 ± 0.09
SN 2017cbv	-12.3	0.44 ± 0.31	78.39 ± 1.34	0.01 ± 0.00
SN 2012dn	-14.4	3.52 ± 0.18	4.07 ± 0.08	0.86 ± 0.05
SN 2012dn	-13.0	27.13 ± 1.07	35.31 ± 0.80	0.77 ± 0.03
SN 2012dn	-10.4	2.19 ± 0.18	3.66 ± 0.12	0.60 ± 0.05
SN 2020esm	-11.8	72.46 ± 2.22	14.79 ± 1.67	4.90 ± 0.57
SN 2020esm	-9.9	50.25 ± 2.80	8.87 ± 2.94	5.67 ± 1.91
iPTF14atg	-11.1	20.30 ± 0.81	35.50 ± 0.91	0.57 ± 0.03

(This table is available in machine-readable form in the [online article](#).)

ORCID iDs

Jialian Liu  <https://orcid.org/0009-0000-0314-6273>
 Xiaofeng Wang  <https://orcid.org/0000-0002-7334-2357>
 Cristina Andrade  <https://orcid.org/0009-0004-9687-3275>
 Pierre-Alexandre Duverne  <https://orcid.org/0000-0002-3906-0997>
 Felipe Navarete  <https://orcid.org/0000-0002-0284-0578>
 Andrea Reguitti  <https://orcid.org/0000-0003-4254-2724>
 Stefan Schuldt  <https://orcid.org/0000-0003-2497-6334>
 Yongzhi Cai  <https://orcid.org/0000-0002-7714-493X>
 Alexei V. Filippenko  <https://orcid.org/0000-0003-3460-0103>
 Thomas G. Brink  <https://orcid.org/0000-0001-5955-2502>
 WeiKang Zheng  <https://orcid.org/0000-0002-2636-6508>
 Ali Esamdin  <https://orcid.org/0000-0003-1845-4900>
 Abdusamatjan Iskandar  <https://orcid.org/0009-0003-9229-9942>
 Jinzhong Liu  <https://orcid.org/0000-0002-7420-6744>
 Xin Li  <https://orcid.org/0000-0001-5879-8762>
 Maokai Hu  <https://orcid.org/0000-0003-3031-6105>
 Wenxiong Li  <https://orcid.org/0000-0002-0096-3523>
 Shengyu Yan  <https://orcid.org/0009-0004-4256-1209>
 Christophe Adami  <https://orcid.org/0000-0002-8904-3925>
 Dalya Akl  <https://orcid.org/0009-0006-4358-9929>
 Eric Broens  <https://orcid.org/0000-0003-1523-4478>
 Eslam Elhosseiny  <https://orcid.org/0000-0002-9751-8089>
 Thomas M. Esposito  <https://orcid.org/0000-0002-0792-3719>
 Michael Freeberg  <https://orcid.org/0009-0005-4287-7198>
 Sergey Karpov  <https://orcid.org/0000-0003-0035-651X>
 Isabel Márquez  <https://orcid.org/0000-0003-2629-1945>
 Martin Mašek  <https://orcid.org/0000-0002-0967-0006>
 Marc Serrau  <https://orcid.org/0009-0003-5793-4293>
 Oleksii Sokoliuk  <https://orcid.org/0000-0003-4503-7272>
 Ali Takey  <https://orcid.org/0000-0003-1423-5516>
 Damien Turpin  <https://orcid.org/0000-0003-1835-1522>

References

- Ahumada, R., Allende Prieto, C., Almeida, A., et al. 2020, *ApJS*, 249, 3
 Aivazyan, V., Almualla, M., Antier, S., et al. 2022, *MNRAS*, 515, 6007
 Altavilla, G., Fiorentino, G., Marconi, M., et al. 2004, *MNRAS*, 349, 1344
 Antier, S., Agayeva, S., Aivazyan, V., et al. 2020a, *MNRAS*, 492, 3904
 Antier, S., Agayeva, S., Almualla, M., et al. 2020b, *MNRAS*, 497, 5518
 Aouad, C. J., Mazzali, P. A., Ashall, C., Tanaka, M., & Hachinger, S. 2024, *MNRAS*, 529, 3838
 Arrizabalaga-Díaz-Caneja, C., Eguiguren-Arrizabalaga, P., Lamolda-Mir, S., et al. 2023, *TNSAN*, 296, 1
 Bai, C.-H., Feng, G.-J., Zhang, X., et al. 2020, *RAA*, 20, 211
 Benetti, S., Cappellaro, E., Mazzali, P. A., et al. 2005, *ApJ*, 623, 1011
 Blondin, S., Dessart, L., Hillier, D. J., & Khokhlov, A. M. 2013, *MNRAS*, 429, 2127
 Boone, K., Aldering, G., Antilogus, P., et al. 2021, *ApJ*, 912, 71
 Branch, D., Fisher, A., & Nugent, P. 1993, *AJ*, 106, 2383
 Branch, D., Dang, L. C., Hall, N., et al. 2006, *PASP*, 118, 560
 Brennan, S. J., & Fraser, M. 2022, *A&A*, 667, A62
 Burns, C. R., Ashall, C., Contreras, C., et al. 2020, *ApJ*, 895, 118
 Burns, C. R., Stritzinger, M., Phillips, M. M., et al. 2011, *AJ*, 141, 19
 Cao, Y., Kulkarni, S. R., Howell, D. A., et al. 2015, *Natur*, 521, 328
 Chakraborty, S., Sadler, B., Hoefflich, P., et al. 2024, *ApJ*, 969, 80
 Chambers, K. C., Magnier, E. A., Metcalfe, N., et al. 2016, arXiv:1612.05560
 Cortés, J. R., Kenney, J. D. P., & Hardy, E. 2008, *ApJ*, 683, 78
 Desai, D. D., Kochanek, C. S., Shappee, B. J., et al. 2024, *MNRAS*, 530, 5016
 Dessart, L., Blondin, S., Hillier, D. J., & Khokhlov, A. 2014, *MNRAS*, 441, 532
 Dessart, L., & Hillier, D. J. 2005a, *A&A*, 437, 667
 Dessart, L., & Hillier, D. J. 2005b, *A&A*, 439, 671
 Dimitriadis, G., Foley, R. J., Arendse, N., et al. 2022, *ApJ*, 927, 78
 Dimitriadis, G., Foley, R. J., Rest, A., et al. 2019, *ApJL*, 870, L1
 Fan, Y.-F., Bai, J.-M., Zhang, J.-J., et al. 2015, *RAA*, 15, 918
 Ferretti, R., Amanullah, R., Goobar, A., et al. 2017, *A&A*, 606, A111
 Filippenko, A. V. 1997, *ARA&A*, 35, 309
 Filippenko, A. V., Richmond, M. W., Branch, D., et al. 1992b, *AJ*, 104, 1543
 Filippenko, A. V., Richmond, M. W., Matheson, T., et al. 1992a, *ApJL*, 384, L15
 Firth, R. E., Sullivan, M., Gal-Yam, A., et al. 2015, *MNRAS*, 446, 3895
 Foreman-Mackey, D., Hogg, D. W., Lang, D., & Goodman, J. 2013, *PASP*, 125, 306
 Gaia Collaboration, Montegriffo, P., Bellazzini, M., et al. 2023, *A&A*, 674, A33
 Gamezo, V. N., Khokhlov, A. M., & Oran, E. S. 2005, *ApJ*, 623, 337
 Ganeshalingam, M., Li, W., Filippenko, A. V., et al. 2012, *ApJ*, 751, 142
 Garavini, G., Folatelli, G., Goobar, A., et al. 2004, *AJ*, 128, 387
 Gehrels, N., Chincarini, G., Giommi, P., et al. 2004, *ApJ*, 611, 1005
 Godson, B., Killestein, T., Ackley, K., et al. 2023, *TNSR*, 2849, 1
 Harris, C. R., Millman, K. J., van der Walt, S. J., et al. 2020, *Natur*, 585, 357
 Hillebrandt, W., & Niemeyer, J. C. 2000, *ARA&A*, 38, 191
 Hoogendam, W. B., Shappee, B. J., Brown, P. J., et al. 2024, *ApJ*, 966, 139
 Hosseinzadeh, G., Sand, D. J., Valenti, S., et al. 2017, *ApJL*, 845, L11
 Howell, D. A., Sullivan, M., Nugent, P. E., et al. 2006, *Natur*, 443, 308
 Hsiao, E. Y., Conley, A., Howell, D. A., et al. 2007, *ApJ*, 663, 1187
 Hu, M., Wang, L., Wang, X., & Wang, L. 2023, *MNRAS*, 525, 246
 Huang, F., Li, J.-Z., Wang, X.-F., et al. 2012, *RAA*, 12, 1585
 Hunter, J. D. 2007, *CSE*, 9, 90
 IRSA 2022, Zwicky Transient Facility Image Service, IPAC, doi:10.26131/IRSA539
 Jha, S., Kirshner, R. P., Challis, P., et al. 2006, *AJ*, 131, 527
 Jiang, J.-a., Doi, M., Maeda, K., & Shigeyama, T. 2018, *ApJ*, 865, 149
 Kann, D. A., Agayeva, S., Aivazyan, V., et al. 2023, *ApJL*, 948, L12
 Karpov, S., 2021 STDPipe: Simple Transient Detection Pipeline, Astrophysics Source Code Library, ascl:2112.006
 Kasen, D. 2010, *ApJ*, 708, 1025
 Kowalski, M., Rubin, D., Aldering, G., et al. 2008, *ApJ*, 686, 749
 Krisciunas, K., Hastings, N. C., Loomis, K., et al. 2000, *ApJ*, 539, 658
 Leibundgut, B., Kirshner, R. P., Phillips, M. M., et al. 1993, *AJ*, 105, 301
 Li, L., Zhai, Q., Zhang, J., & Wang, X. 2023, *TNSCR*, 2870, 1
 Li, W., Wang, X., Vinkó, J., et al. 2019, *ApJ*, 870, 12
 Lira, P., Suntzeff, N. B., Phillips, M. M., et al. 1998, *AJ*, 115, 234
 Macri, L. M., Calzetti, D., Freedman, W. L., et al. 2001, *ApJ*, 549, 721
 Maeda, K., Jiang, J.-a., Doi, M., Kawabata, M., & Shigeyama, T. 2023, *MNRAS*, 521, 1897
 Magee, M. R., & Maguire, K. 2020, *A&A*, 642, A189
 Marion, G. H., Brown, P. J., Vinkó, J., et al. 2016, *ApJ*, 820, 92
 Matheson, T., Kirshner, R. P., Challis, P., et al. 2008, *AJ*, 135, 1598
 Mazzali, P. A., Danziger, I. J., & Turatto, M. 1995, *A&A*, 297, 509
 Mazzali, P. A., Sullivan, M., Hachinger, S., et al. 2014, *MNRAS*, 439, 1959
 Miller, A. A., Cao, Y., Piro, A. L., et al. 2018, *ApJ*, 852, 100
 Miller, J. S., & Stone, R. P. S. 1994, The Kast Double Spectrograph, Lick Observatory Technical Reports 66, Univ. of California
 Moriya, T. J., Mazzali, P. A., Ashall, C., & Pian, E. 2023, *MNRAS*, 522, 6035
 Mould, J. R., Huchra, J. P., Freedman, W. L., et al. 2000, *ApJ*, 529, 786
 Murakami, Y. S., Riess, A. G., Stahl, B. E., et al. 2023, *JCAP*, 2023, 046
 NASA/IPAC Extragalactic Database (NED) 2019, NASA/IPAC Extragalactic Database (NED), IPAC
 Nomoto, K., Iwamoto, K., & Kishimoto, N. 1997, *Sci*, 276, 1378
 Nugent, P. E., Sullivan, M., Cenko, S. B., et al. 2011, *Natur*, 480, 344
 Oke, J. B., Cohen, J. G., Carr, M., et al. 1995, *PASP*, 107, 375
 Pakmor, R., Kromer, M., Taubenberger, S., et al. 2012, *ApJL*, 747, L10
 Pan, Y. C., Foley, R. J., Kromer, M., et al. 2015, *MNRAS*, 452, 4307
 Parent, J. T., Howell, D. A., Fesen, R. A., et al. 2016, *MNRAS*, 457, 3702
 Perley, D. A. 2019, *PASP*, 131, 084503
 Perlmutter, S., Aldering, G., Goldhaber, G., et al. 1999, *ApJ*, 517, 565
 Phillips, M. M. 1993, *ApJL*, 413, L105
 Phillips, M. M., Ashall, C., Burns, C. R., et al. 2022, *ApJ*, 938, 47
 Phillips, M. M., Lira, P., Suntzeff, N. B., et al. 1999, *AJ*, 118, 1766
 Phillips, M. M., Simon, J. D., Morrell, N., et al. 2013, *ApJ*, 779, 38
 Phillips, M. M., Wells, L. A., Suntzeff, N. B., et al. 1992, *AJ*, 103, 1632
 Piro, A. L., & Morozova, V. S. 2016, *ApJ*, 826, 96
 Piro, A. L., & Nakar, E. 2014, *ApJ*, 784, 85
 Poznanski, D., Prochaska, J. X., & Bloom, J. S. 2012, *MNRAS*, 426, 1465
 Riess, A. G., Filippenko, A. V., Challis, P., et al. 1998, *AJ*, 116, 1009
 Riess, A. G., Macri, L. M., Hoffmann, S. L., et al. 2016, *ApJ*, 826, 56
 Riess, A. G., Yuan, W., Macri, L. M., et al. 2022, *ApJL*, 934, L7
 Roming, P. W. A., Kennedy, T. E., Mason, K. O., et al. 2005, *ssr*, 120, 95
 Sasdelli, M., Mazzali, P. A., Pian, E., et al. 2014, *MNRAS*, 445, 711
 Savitzky, A., & Golay, M. J. E. 1964, *AnaCh*, 36, 1627
 Scalzo, R., Aldering, G., Antilogus, P., et al. 2012, *ApJ*, 757, 12
 Scalzo, R., Aldering, G., Antilogus, P., et al. 2014, *MNRAS*, 440, 1498

- Schlafly, E. F., & Finkbeiner, D. P. 2011, *ApJ*, 737, 103
- Shappee, B. J., Holoiien, T. W. S., Drout, M. R., et al. 2019, *ApJ*, 870, 13
- Siebert, M. R., Kwok, L. A., Johansson, J., et al. 2024, *ApJ*, 960, 88
- Silverman, J. M., Ganeshalingam, M., Cenko, S. B., et al. 2012a, *ApJL*, 756, L7
- Silverman, J. M., Foley, R. J., Filippenko, A. V., et al. 2012b, *MNRAS*, 425, 1789
- Smitka, M. T., Brown, P. J., Suntzeff, N. B., et al. 2015, *ApJ*, 813, 30
- Stahl, B. E., Zheng, W., de Jaeger, T., et al. 2019, *MNRAS*, 490, 3882
- Stahl, B. E., Zheng, W., de Jaeger, T., et al. 2020, *MNRAS*, 492, 4325
- Stritzinger, M., & Leibundgut, B. 2005, *A&A*, 431, 423
- Stritzinger, M., Hamuy, M., Suntzeff, N. B., et al. 2002, *AJ*, 124, 2100
- Taubenberger, S. 2017, in *Handbook of Supernovae*, ed. A. W. Alsabti & P. Murdin (Berlin: Springer), 317
- Virtanen, P., Gommers, R., Oliphant, T. E., et al. 2020, *NatMe*, 17, 261
- Wang, C.-J., Bai, J.-M., Fan, Y.-F., et al. 2019, *RAA*, 19, 149
- Wang, L., Contreras, C., Hu, M., et al. 2020, *ApJ*, 904, 14
- Wang, X., Wang, L., Filippenko, A. V., Zhang, T., & Zhao, X. 2013, *Sci*, 340, 170
- Wang, X., Li, W., Filippenko, A. V., et al. 2008, *ApJ*, 675, 626
- Wang, X., Filippenko, A. V., Ganeshalingam, M., et al. 2009, *ApJL*, 699, L139
- Yang, J., Wang, L., Suntzeff, N., et al. 2022, *ApJ*, 938, 83
- Yaron, O., Young, D., Smith, K., & Smartt, S. 2023, *TNSAN*, 112, 1
- Zhai, Q., Zhang, J.-J., Wang, X.-F., et al. 2016, *AJ*, 151, 125
- Zhang, J.-C., Fan, Z., Yan, J.-Z., et al. 2016a, *PASP*, 128, 105004
- Zheng, W., Silverman, J. M., Filippenko, A. V., et al. 2013, *ApJL*, 778, L15
- Zhang, K., Wang, X., Zhang, J., et al. 2016b, *ApJ*, 820, 67